Chapter 5

Single-Pulse Studies : Polar Maps of Pulsars B0943+10 and B0834+06

In the last chapter, we dwelled on the fluctuation properties of a few bright pulsars observable using GEETEE at 35 MHz. We now attempt to study a subset of that data in greater detail and to try to understand the observed diverse single-pulse fluctuation properties in terms of polar emission patterns and their temporal behavior. We compare our observations with the general picture of radio emission elaborated theoretically by Goldreich & Julian, 1970 (hereafter GJ), Sturrock, 1971, and Ruderman & Sutherland, 1975 (hereafter R&S).

For such a study we have chosen two pulsars, *viz.* B0943+10 and B0834+06. These two bright pulsars exhibit strong fluctuations. PSR0943+10 is indeed a unique pulsar for it is among a handful of pulsars discovered in surveys conducted at frequencies below 400 MHz, and displays an unusually steep spectrum above 100 MHz. It was only recently detected at 800 MHz and 1400 MHz after immense efforts (Deshpande et al., 1999, and Weisberg et al., 1999). As Deshpande & Rankin, 1999 (DRa), point out, the 430-MHz observations sample the outer $\leq$ 50% of the radial extent of the subbeams defining the hollow cone of emission, and DRa believe this to be the cause for its steep spectrum. It is certainly of interest to study single-pulse sequences from this pulsar at decameter wavelengths, where it is expected to be relatively bright. From the radius-to-frequency mapping (section 1.1.3), and the generally assumed dipole-field geometry, we expect to sample the emission region at low frequency more centrally and thus more completely, and resolve the high frequency 'single' profile into a "double". This is clearly advantageous for estimating the profile center (*i.e.* corresponding to the longitude of the magnetic axis), which is an important input in using "Cartographic Transform" technique, an issue that we deal with later. Also of interest will be the character of the emission pattern at low frequencies, as this emission is believed to originate farther away from the surface of the star (*i.e.* RFM), where the toroidal component

due to particle currents could become relevant. B0834+06 shows a double component profile, and displays fluctuations which are not as steady as B0943+10. B0834+06 also has the well known alternate pulse modulation, without any significant drift at higher frequencies. This offers us a useful case to illustrate that different forms of single-pulse modulation discussed in section 1.2 could be viewed in an unified manner. For both these pulsars we could estimate the subbeam circulation time ($\hat{P}_3$) directly based on fluctuation-spectral analysis. Using our estimates of $\hat{P}_3$ and the available estimates of pulsar geometry in the literature, we have obtained average polar-emission maps for these pulsars. These and other results are presented in this chapter[1].

To start with, we discuss the R&S model specifically in some detail, and compare the theoretical and observational estimates regarding the subpulse drift. We discuss the observed fluctuation spectra and our methods of estimating $\hat{P}_3$, followed by the details of the "Cartographic Transforms" and related issues of mapping. We present polar maps, for the two pulsars made from various available data sets in the decameter band, and also look at sensitivity to various assumptions and parameters. Lastly, we compare these results with high radio-frequent$ observations, seeking some insights into radio-emission mechanisms.

5.1 Ruderman & Sutherland (R&S) model

As yet, physical origin of pulsar radio emission is still not understood adequately. Models with dipole magnetic field-geometry connecting the average-pulse shape and polarization properties were proposed almost immediately after the discovery of pulsars (Radhakrishnan & Cooke, 1969 — hereafter RC), making use of the suggestions by GJ. GJ proposed an electrodynamics solution for a homo-polar rotator, which illustrated some underlying principles about the physical conditions around a pulsar. Some later attempts toward "comprehensive" solutions (R&S, Arons & Scharlmann, 1979, Beskin et al.., 1988, etc) followed this approach (by "comprehensive" we mean the set of models which, along with the fundamental emission mechanism, try to relate to most of the crucial observed phenomena). Other theories invoking coherent emission processes have been proposed as well. (Melrose, 1994, Lyutikov et *al.*, 1999)

As mentioned in section 1.1.1, the rotational energy is believed to be carried away by charged-particle bunches along the polar flux tube as well as via low frequency dipole radiation, and there is a general consensus on the fundamental aspects of the polar emission models. However,

[1]Some initial results from this work were presented in IAU-177, "Pulsars - 2000 and beyond", (Asgekar & Deshpande, 2000), and a fuller version about results for the pulsar B0943+10 was published in MNRAS (Asgekar & Deshpande, 2001).

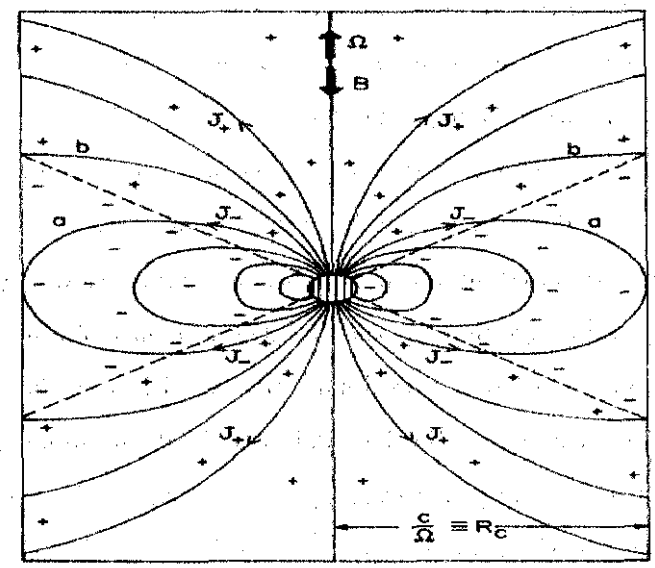

Figure **5.1:** Sketch of the magnetic field lines, currents, and magnetospheric charge density for a GJ model in which the rotation and magnetic dipole axes are anti-parallel. The magnetic field assumed to be purely dipolar. The dashed lines represent the charge separation in the non-co-rotating magnetosphere. From the equator to the pole: Line a is the last one to close within the light cylinder; Lines between a and b are open and pass through regions of negative charge as they cross the light cylinder. Open magnetic field lines between b and the pole pass through the regions of positive charge.

no theory explains every detail observed. Almost all fail to describe some of the observed average and single-pulse properties described in sections **1.1.3** and **1.2.** Our aim is to relate the observed phenomena of subpulse drift with the corresponding theoretical estimates, and R&S remains as the only model that provides a physical basis for the subpulse-drift process.

5.1.1 Goldreich-Julian result

GJ pointed out, that despite the star's intense gravity, the star must possess a dense magnetosphere due to strong electrodynamic forces. They elucidated the characteristics of the co-rotating magnetosphere surrounding an axisymmetric neutron star with aligned magnetic and rotation axes. They assumed that (a) the neutron star (here after NS) can supply the necessary charges of either sign to fill and maintain the magnetosphere with a vanishing net component of electric field parallel to magnetic field, and (b) the currents in the magnetosphere are negligible. We refer to the schematic of this picture in the figure **5.1.** The magnetic field (B), and the angular velocity of the NS (Ω) are antiparallel as shown. The co-rotating magnetosphere charge density is given by

$$\rho_e = -\frac{\mathbf{\Omega}.\mathbf{B}}{2\pi c} \frac{1}{(1 - \Omega^2 r_\perp{}^2/c^2)}, \tag{5.1}$$

where $r_\perp = r sin\theta$, r is the radial coordinate, *6* is the polar angle, and c is the speed of light (a result is shown valid also in the case where the two axes are not aligned). In the stationary observer's frame, the electric field is given by,

$$\mathbf{E} = -(\mathbf{\Omega} \times \mathbf{r}) \times \mathbf{B}/c \tag{5.2}$$

In the approximation that the magnetic field contribution from magnetospheric currents is negligible, the magnetic field far away from the NS surface is dominated by the star's dipole field. Those field lines which originate sufficiently close to the polar caps will cross the light cylinder of radius

$$R_{LC} \equiv c/\Omega \tag{5.3}$$

at which co-rotation can no longer be maintained. These field lines define two "polar caps" on the stellar surface from which charges leaving the star follow the field lines and escape from the co-rotating magnetosphere. In a pure dipole approximation, the radius of such a polar cap region from which charges move out is given by

$$r_p = \left(\frac{2}{3}\right)^{3/4} R\left(\frac{\Omega R}{c}\right)^{1/2} \approx 10^4 P^{-1/2} cm \tag{5.4}$$

where R is the stellar radius, taken to be 10 Km. This model anticipates charge separation, and a (centrifugally induced) loss of charged particles out through the light cylinder would cause $\mathbf{E} \cdot \mathbf{B} \neq 0$ near the stellar surface. This model is elaborated in the figure 5.1. The potential difference between the center of the polar cap and the edge of the negative current emission is given by

$$\Delta V \approx \frac{\Omega^2 R^3}{2c^2}(\mathbf{B}_s{}^d \cdot \mathbf{r}) \tag{5.5}$$

$$\approx 3.3 \times 10^{12} B_{12}/P^2 volts, \tag{5.6}$$

assuming only the magnetic dipole contribution $(\mathbf{B}_s^d)$ to the surface magnetic field (B,).

The maximum net charged particle flux from the polar cap is, from eq. 5.1,

$$\dot{N}_{max} \approx \pi {r_p}^2 \frac{\mathbf{\Omega} \cdot \mathbf{B_s}}{2\pi ec}. \tag{5.7}$$

This current results in a braking torque on the spinning star and reduces the stellar rotation energy at a rate

$$\frac{dE}{dt} \approx \frac{(\dot{B}_s{}^d)^2 \Omega^4 R^6}{c^3}. \tag{5.8}$$

This equation then forms the basis for estimating the surface magnetic field using the measured values of period and its slowdown rate.

5.1.2 Gap formation and particle avalanche

The major standpoint of the R&S model is about the structure of the NS crust matter in the presence of ultra-high magnetic fields ($\approx 10^{12}$G) (Ruderman, 1974; Chen, Ruderman, & Sutherland, 1974). Their calculations yielded a binding energy per ion ~ 14 keV, which is much higher than electron Fermi energy of ~ 750 eV. So they invoked two postulates: (1) The electrons, which move through the light cylinder, do not easily flow back through the light cylinder into the co-rotating magnetosphere; (2) The NS surface is a copious supplier of electrons, but not of positive ions (The electric fields near the surface are not strong enough to "pull out" the ions). R&S work out the case of a NS with rotation and magnetic axes anti-parallel to each other, where the charge signs are reversed (positrons instead of electrons and vice versa).

Here again the magnetospheric charge density is given by eq. 5.1, but the angular frequency of the charges (Ω) is less than that of the NS (R^*). The magnetosphere is separated from the star by a spherical gap of height h, and the two rotation periods are related by,

$$\frac{\Omega^*}{\Omega(h)} = 3/5\left(\frac{(R+h)^2}{R^2} + \frac{2}{3}\frac{R^3}{(R+h)^3}\right) \tag{5.9}$$

$$1 + \frac{3h^2}{R^2} \quad (h \ll R). \tag{5.10}$$

For a dipolar magnetic field, the electric field and associated charge density in the magnetosphere are quadrupolar and exactly that of a normal magnetosphere rotating at Ω; in the NS, the electric field is $\mathbf{E} = -(\mathbf{\Omega}^* \times \mathbf{r}) \times \mathbf{B}/c$. Within the gap $\mathbf{E} \cdot \mathbf{B} \neq 0$, but it vanishes at the base of the magnetosphere. At the pole the gap electric field at the NS is normal to the stellar surface, and is given by

$$E_p = \frac{2\Omega^* B}{c} h \qquad (h \ll R); \tag{5.11}$$

and the potential across the gap at the pole is

$$\Delta V = \frac{\Omega^* B}{c} h^2. \tag{5.12}$$

A case of physical interest occurs in the gap formed, when positive charge flows out along the open field lines emanating from the polar cap of radius r_p and there is no charge replacement from the stellar surface (figure 5.2). The gap thickness will grow at a speed near c if the outward flow of positive charge through the light cylinder approaches to the maximum permitted by eq. 5.1. But the potential difference across the gap increases as h^2. Such a gap is unstable against charge particle avalanche. In the huge gap magnetic field any γ-ray particle with energy significantly higher

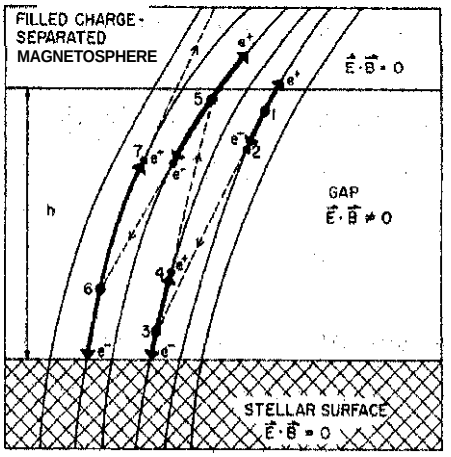

Figure 5.2: Breakdown of the polar gap. The solid lines are polar field lines of average radius of curvature p $\sim 10^6$ cm for a realistic case, with higher multi-pole contributions, which could be significant near the star. A photon (of energy $\geq 2mc^2$) could produce a charge pair at 1. The positron is accelerated out of the gap, whereas the electron is accelerated toward the stellar surface. The electron moves along a curved field line, which then radiates an energetic photon at 2, which again goes on to produce a charge pair, once it has a sufficient component of its momentum perpendicular to the magnetic field. This, under appropriate conditions, could result in a runaway cascade, which then breaks down the gap.

than 2m,c^2 may generate an $e^- - e^+$ pair. (Shukre & Radhakrishnan, 1982, considered "triggering" of such a gap by the background gamma-ray radiation, and interestingly found it effective only in a small "window" of magnetic field strengths centered on 2.5 x 10^{12}G). These "primary" particles are accelerated in the gap and emit "curvature radiation" of characteristic frequency

$$\omega \approx \frac{3}{2}\frac{\gamma^3 c}{\rho} \tag{5.13}$$

where p is the radius of curvature of the field line along which the e^-/e^+ charges of energy γmc^2 move. For e^-/e^+ charges which have been accelerated to energies $e\Delta V \geq 10^{11}$ eV, these 'curvature photons' may lead to additional pair charge creation. The condition that curvature radiation photons produce a pair in the gap (radiation losses), from the mean free path considerations, leads to

$$h \approx 5 \times 10^3 \rho_6^{2/7} P^{3/7} B_{12}^{-4/7} cm \tag{5.14}$$

for the gap height, where $B_{12}=\hat{\mathbf{r}}\cdot\mathbf{B}_s/10^{12}$G, $\rho_6 = \rho/10^6$cm, and P is the pulsar rotation period. R&S assume in all their calculations $\rho_6 \sim 1$, which would not be the case for a strictly dipolar field. In this case, the presence of multi-polar components is assumed, which will contribute strongly only near the surface. With this, the gap potential difference is given by

$$\Delta V = \frac{\Omega B_s h^2}{} \tag{5.15}$$

$$= 1.6 \times 10^{12} B_{12}^{-1/7} P^{-1/7} \rho_6^{4/7} volts. \quad (5.16)$$

With this potential difference, one expects relativistic $e^- - e^+$ pairs with $\gamma \sim 3 \times 10^6$. The component of the electric field along the magnetic field is

$$E \simeq \frac{2\Omega B_s}{c}(h - z), \quad (5.17)$$

which vanishes at the top of the gap. At the bottom, the potential difference $\sim 10^9$ volts is much less than that required to pull ions away from the surface. R&S argue that the curvature radiation from the "primary" particles can lead to a pair cascade, leading to a discharge of the gap once h grows to a value determined by eq. 5.14.

The upper bound for the energy flux carried by relativistic positrons into the magnetosphere above the gap is

$$E_{+max} \approx e \Delta V \rho_e c \pi r_p^2 \quad (5.18)$$

$$\approx 10^{30} B_{12}^{6/7} \rho_6^{4/7} P^{-15/7} erg/s \quad (5.19)$$

where, B_{12} is the magnetic field in the units of 10^{12} G, and ρ_6 is the radius of curvature of the field lines in 10^6 cm.

5.1.3 Mechanism of radio emission : plasma instability and bunching

R&S argue that most of the high energy positrons created in the gap $\left(\gamma \approx \gamma_{max} = \frac{e\Delta V}{m_e c^2} [eq.\ 5.12]\right)$ do not undergo any further acceleration and spend their entire energy in generating "secondary" pairs in the near magnetosphere. Incoherent curvature radiation from the charged particles and their relative motion does not explain the observed pulsar fluxes. At the same time, the high brightness temperatures observed in the radio emission indicate some coherent mechanism at work. R&S invoke a two-stream instability within the secondary relativistic pair plasma stream ($\gamma \approx 800$), which results in bunching of the radiating charges. They argued that this results in coherent curvature radiation from the charge bunches.

We do not wish to go into these details as they are rather irrelevant for our purpose here. Serious doubts have been raised about effectiveness of the bunching process and the growth rate of such an instability (later approaches try to resolve these in various manners) as well. Indeed, the model has been severely criticized on various grounds. But, this model has provided us with a picture of the rotating subbeams of emission in the polar regions of a pulsar. This picture is very well supported by our single-pulse analysis (and that by Deshpande & Rankin as well), even

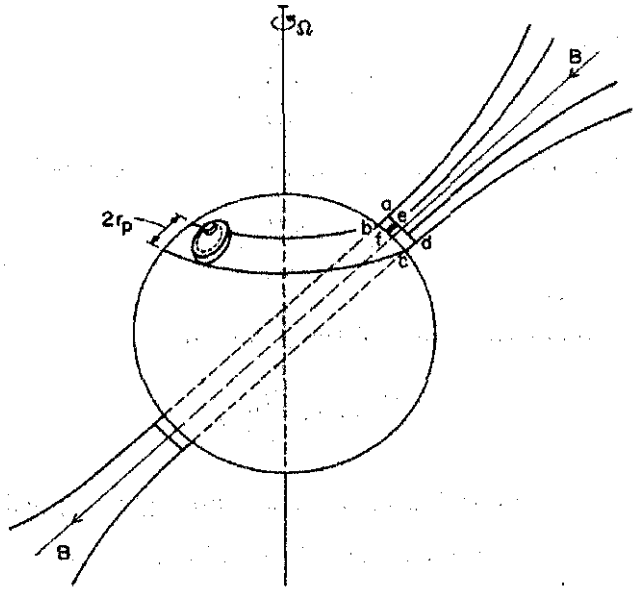

Figure 5.3: Schematic of an oblique rotator. The polar cap, of base diameter $2r_p$, moves at fixed latitude. A spark ef in the gap *abcd* drifts clockwise on a circular path (dashed line) on the polar cap centered on the magnetic field axis. This spark feeds relativistic particles onto field lines: coherent microwave radiation is produced tangentially to these field lines far above the stellar surface.

though the detailed mechanism is yet unclear. We, therefore, describe this aspect of the model in detail.

5.1.4 Structure and drifting of sparks

After the discharge, the value of $\mathbf{E} \cdot \mathbf{B}$ falls rapidly at the location of the discharge in the polar gap. This would be expected to inhibit the formation of another simultaneous discharge within a distance $\sim$ h, the gap height. Thus, the gap discharges through a group of localized or discrete "sparks". These sparks inject energetic positron beams into the magnetosphere beyond the gap. The positrons are argued to convert their energy into a cascade of "secondary plasma", which in turn emits coherent microwave radiation. Regardless of the actual mechanism of this conversion, the location of the sparks on the polar cap is believed to determine the observed temporal behavior of subpulses within a pulsar's average pulse window. The intensity of the spark discharge may fluctuate, but presumably it rarely turns off entirely. Electrons and positrons in a spark do not exactly co-rotate with the stellar surface until $\mathbf{E} \cdot \mathbf{B} = 0$ everywhere along the discharge.

A schematic of the related geometry is shown in figure **5.3.** Magnetic field within the gap is simplified to being constant in magnitude, and normal to stellar surface. The occurrence of the gap discharge changes the electric field within the gap, which alters the co-rotation velocity $(\frac{\mathbf{E}\times\mathbf{B}}{B^2}c)$.

R&S derive the average magnitude of the drift velocity of the sparks around the magnetic pole at an assumed radius of $r_p/2$ as

$$\delta v = \frac{\Delta V}{B_s r_p} c \tag{5.20}$$

The time taken to complete one revolution around the magnetic axis is,

$$\hat{P_3} = \frac{\pi B_s r_p^2}{\Delta V c}, \tag{5.21}$$

and hence, for spark location at the center of the polar cap,

$$\frac{\hat{P_3}}{P} \approx 3.6 \frac{B_{12}}{P^2}\ s, \tag{5.22}$$

where P is in seconds, R = 10^6 cm, radius of the polar cap is given by eq. 5.4 and AV = 10^{12} volts. We refer to figure 5.11 for a schematic of observed subpulse drift pattern. The period of recurrence of subpulses at a particular longitude, P_3, is expected to be related to $\hat{P_3}$ as

$$P_3 \approx \hat{P_3}/n, \tag{5.23}$$

where n is the total number of spark discharges around the polar cap (We shall argue later, that $\hat{P_3}$ is constant for a given pulsar and is expected to be of more fundamental significance than P_3). The period P_2, the subpulse spacing, has a natural meaning in this picture as well, in terms of the distance between sparks (s). Assuming emission from coherent radiation from spark-induced bunches to be tangential to the local magnetic field lines, the relation for P_2 reads

$$\left(\frac{s}{r_p}\right) \sim \frac{P_2}{P}\left(\frac{360^\circ}{\theta_\omega}\right), \tag{5.24}$$

where θ_ω is the observed average-pulse width of the pulsar.

R&S present calculations of photon conversion rate, and growth and fluctuation rate of the sparks. The fluctuation scale of a spark discharge is argued to be $\sim 10\mu sec.$ This is compared with the observed micro-structure in pulsar data, with the subpulse defining the smooth envelop of such a microstructure.

5.1.5 Comparison with observations

Radio luminosity & spectrum

The pulsar radio luminosity is believed to be a tiny fraction of the total energy loss and hence, is loosely bounded, from eq. 5.19 as,

$$L_{radio} < L_{max} = 10^{30} P^{-\frac{15}{7}} erg/s, \tag{5.25}$$

which is not inconsistent with observations.

Assuming dipole field geometry, R&S arrive at limits for the size of the polar emission region (x) from the center at a radial distance from the star (r) as,

$$x^2 \leq (2/3)^{3/2} \frac{\Omega r^3}{c}, \tag{5.26}$$

and

$$x \geq \frac{16}{9\gamma_{\pm}{}^3 c} \left(\frac{2\gamma_{max}\, e\Omega B R^3}{mc} \right)^{1/2} r^{1/2}. \tag{5.27}$$

The minimum height of emission region then turns out be $\approx 10^8$cm. The radiation pattern and pulse envelope are expected to be governed by the tangents to the open field lines at the point of emission. With an assumption that radiation occurs only at local plasma frequency, ω_p (*e.g.* via effective bunching occurring very close to ω_p), we get a relation for the height of emission region as

$$r = 2 \left(\frac{\gamma_{max}\, e\Omega B R^3}{mc} \right)^{1/3} \omega^{-2/3}. \tag{5.28}$$

This relation, expressed as the beam angle of radiation $\theta (\propto \sqrt{r})$, gives an analog of the familiar RFM known from observations (section 1.1.3), with $\theta \propto \nu^{-1/3}$.

The upper and lower limits on the radio frequency of emission are derived as well. The limits derived are not very reliable, since they depend upon relatively unknown surface parameters of pulsars, the magnetic field and ρ, the radius of curvature of the magnetic field lines. The model predicts presence of a maximum in the spectrum at a certain frequency between 10 MHz and 1 GHz, on either side of which the pulsar flux declines.

Beam morphology and polarization behavior

Issues related to the structure of pulsar beam shapes and RFM are explained adequately by invoking a simple double-cone or multi-cone geometry (figure 1.7). A simple explanation for the observed pulse shapes, widths, and their frequency evolution is an attractive feature. But, this model fails to explain the "core" component, and the fact that there are two (and only two ?) cones.

Since the emission is tied up with the magnetic field lines, the smooth sweep of polarization angle finds a physically elegant explanation. The open dipole field lines originate on and diverge away from the polar cap. The planes defined by their curvature intersect the line-of-sight as shown in figure 5.4, resulting in the observed pattern of the linear polarization angle. All models which argue similarly fail to anticipate OPMs (section 1.2.5), circulation polarization behavior, and their correlation with other pulsar parameters.

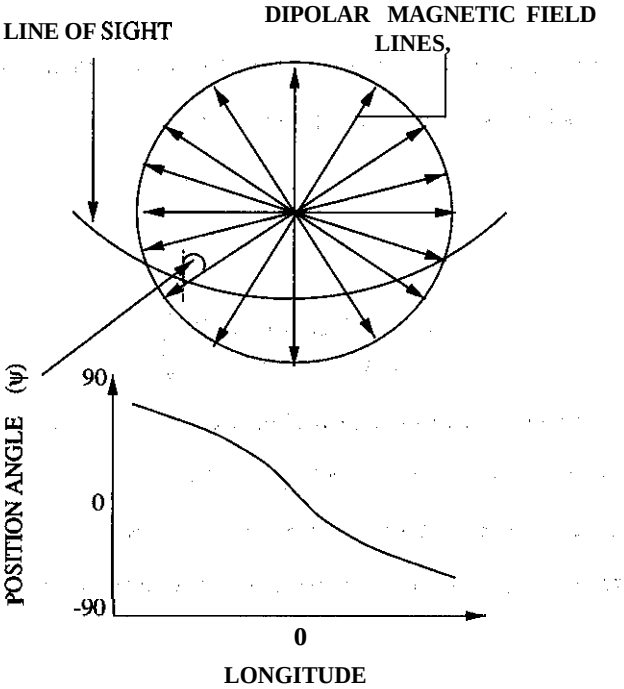

Figure 5.4: Locus of the observer's line-of-sight and the sweep of the linear polarization of the radiation: The polarization-angle depends upon the orientation of the magnetic field lines with the line-of-sight locus. The fastest rate of change of angle is at the center of the profile, which defines the longitude of the magnetic axis.

5.1.6 Circulation time and the number of subbeams

The R&S model explains subpulse drift as a physical drift of the spark discharges around the magnetic axis. The circulation time for such a system around the magnetic axis is given by eq. 5.22. We, however, would like to make a distinction between observed modulation periodicity (P_3) and the circulation time of the entire pattern $(\hat{P}_3)$, which need not follow an integral-multiple relation (eq. 5.23 may only be valid in some pulsars). An integer relationship is possible if the sparks are stable and follow a uniform spacing around the polar cap.

5.1.7 Correlation of P_3 with pulsar parameters

Several multi-frequency studies have shown the fluctuation properties of pulsars to be independent over a wide range of observational frequency (DRa; Nowakowski et *al.*, 1982, and references therein). In particular, P_3 is observed to be frequency independent.

The modulation index of the drift was found to decrease with increasing frequency, and at sufficiently higher frequencies $(\geq 2\ GHz)$ was found to increase again, Bartel, Sieber, & Wolszczan (1980). The contribution of the drift component to the total average pulse energy decreases with increasing frequency, whereas that of the steady component shows a rise.

Wolszczan (1980) reported an observed correlation of P_3 with the magnetic field and age of pulsars (P-B diagram). Both these effects can be understood in terms of the simple spark geometry on the polar cap, and the effect of pulsar evolution on the period-magnetic field diagram with or without magnetic field decay. The estimated values of P_3, and the direction of the drift in the pulse (from spectra or otherwise) can be in significant error due to possible unresolved issues of aliasing. Hence, such a correlation would appear even less reliable.

5.2 The data

Our 34.5 MHz observations lack the sensitivity to detect a majority of the individual pulses in the recorded sequences, let alone view their drift pattern, if any. Any such drift or modulation is hence studied by directly characterizing the average properties of the fluctuation. From our entire set of observations during the years 1997 and 1999, we have identified a total six single-pulse data sets for the pulsar B0943+10 and five for B0834+06. Here we present all the data sets, talk about the data quality, and elaborate our means and ways of deducing $\hat{P}_3$ for these pulsars.

5.2.1 Data quality

Fluctuation spectral analysis is prone to corruption due to low-level radio interference (esp. in a case like ours, where one doesn't have enough sensitivity to detect individual pulses). All data sets were examined for possible interference in the raw radio spectrum (section 1.3.3). As a further check, we also looked at the final time series and its spectrum. Typically, strong interference features at $f \sim 48$ Hz, $f \sim 60$ Hz, or, $f \sim 96$ Hz were present in some data sets, and were removed. For detailed studies, care was taken to make sure that the rest of the fluctuation features were entirely trustworthy, and not an artefact due to instrumental or interference effects.

Fluctuation properties are not expected to change significantly between different sets. But sometimes a few pulse sequences may not show fluctuation properties clearly (in the case of 0834+06 these could be the nulls which are undetectable in our observations), or some occasional ultra strong pulse could dominate the apparent fluctuation behavior. For such reasons and from the signal-to-noise considerations it is found necessary to carefully choose suitable sub-sequences, typically of 128/256/512 pulses, to clarify a point at hand for spectra and the related issues.

Figure 5.2.2 shows a plot of pulse energy variation over a sequence of single pulses from PSR0943+10. Only a few of the strongest pulses are detectable individually, with the noise level being ~ 6 Jy as opposed to the average pulse energy of ~ 9 Jy. The raw fluctuation spectrum for one PSR0943+10 sequence is shown in figure 5.5. The frequency of the features is plotted on the X-axis in units of the fundamental rotational frequency of the star $(2\pi/P_1)$. The harmonics decline by harmonic number 10, and rise again at harmonic number of 16, again decay to half the value at about harmonic number 20. The second peak in the harmonic strengths at harmonic number of 16 corresponds to the longitude separation of peaks of the two components in the average pulse profile (about 20°). Also, notice the spectral components at about half integral frequencies. They represent the subpulse modulation phenomena. The strong and sharp fluctuation features underscore the

stability and power of the process giving rise to these fluctuations. Any contamination from an interfering signal of 48 Hz or 96 Hz could override this spectrum, if it were to be present.

5.2.2 B0943+10

This pulsar displays stable subpulse drift patterns with a steady drift rate. In fact, the very stability of the drift motion has allowed Deshpande & Rankin, and ourselves, to study the process in a new way. B0943+10 belongs to the S_d class of pulsars according to Rankin-IV, and Paper-I has worked out the viewing geometry for this pulsar with multi-frequency data sets. For simplicity of reference we (arbitrarily) refer to our 6 data sets from this pulsar by a unique number between 1 to 6. We estimate, in this section, the circulation time associated with the drift from the observed fluctuation properties, which we later use appropriately for mapping regions of polar emission.

Spectra

We look at the longitude-resolved fluctuation (lrf-) spectrum constructed by using 512 pulses from set-1 (figure 5.7). We concentrate on the strong features at $\sim 0.46\, c/P_1$ (hereafter feature-1) and $-0.027\, c/P_1$ (hereafter feature-2). The feature-1 is associated with the observed subpulse drift at meter wavelengths; it is barely resolved here, implying a Q ($\equiv f/\Delta f$) of $\gtrsim 225$. This clearly indicates that the underlying modulation is steady even at decameter wavelengths. The drift is usually less stable in our data sets, with a Q-value ranging between 100 and 200. One such a example is shown for set-2 in figure 5.8, an lrf-spectrum computed using 128 pulses. The modulation frequency varies slightly between different sets. Such a small variation ($\lesssim 1\%$) was also noted by DRa in higher frequency data, and is not surprising. The important questions we wish to address are the effect of a possible aliasing of feature-1 and the relation between the two features.

Aliasing and the true frequency of the primary modulation

To assess the issue of aliasing, we compute the hrf-spectra using set-1 and set-2, and present them in figures 5.9 and 5.10. As illustrated in section 4.2.2, the asymmetry of the features around $0.5\, c/P_1$ indicates that the fluctuation feature at $0.541\, c/P_1$ is associated with a phase modulation, and appears as a first-order aliased feature-1 at $0.459\, c/P_1$ in the lrf-spectra. A similar conclusion about the nature of the modulation can be drawn by looking at the rate of change of the modulation phase with longitude (see figure 5.12), which is $\sim 26°/°$— too large for a mere amplitude modulation

We now fold the pulse sequence at the primary modulation frequency P_3 noted for different data sets, and such a folded pattern for set-2 is shown in figure 5.12 (also shown is the plot for set-3).

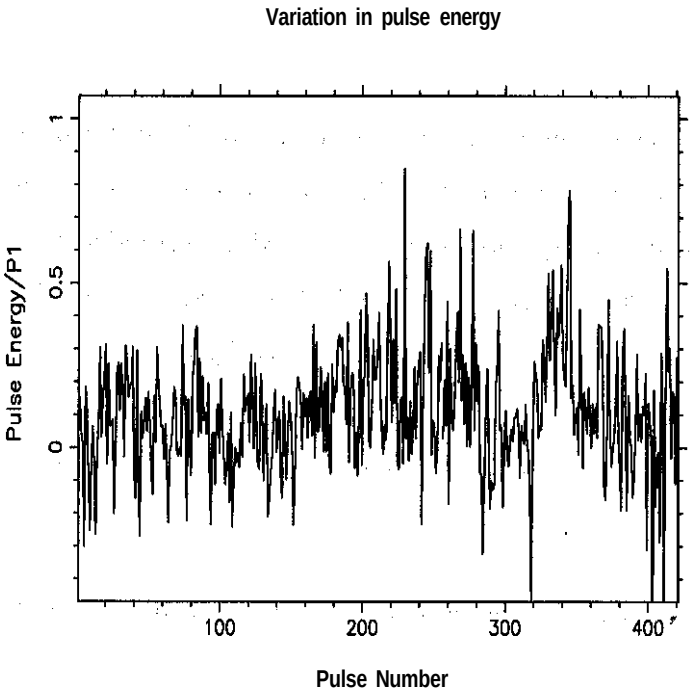

Figure 5.5: Energy variation in a pulse sequence for set-2 of B0943+10 (Units on Y-axis are arbitrary). Only a few strong pulses are detectable individually.

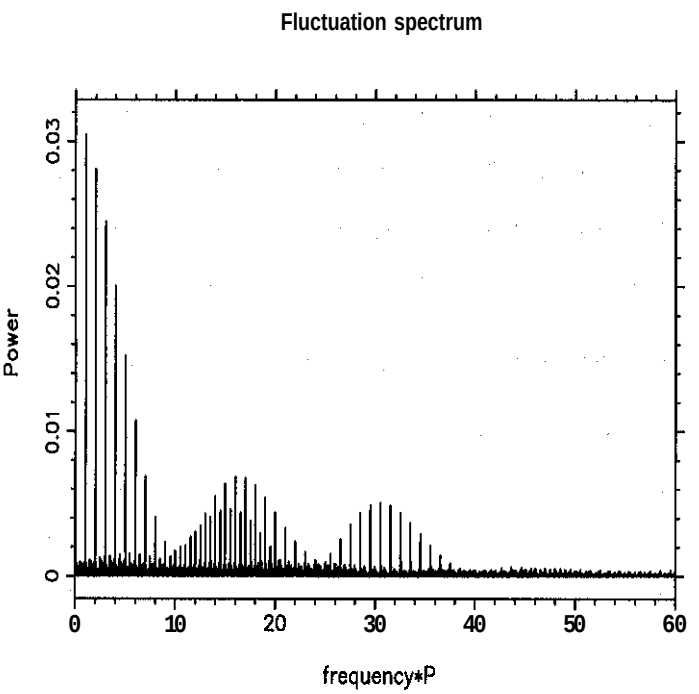

Figure 5.6: Raw fluctuation spectrum for set-2 of B0943+10 (see text and section 4.2.2 for more details).

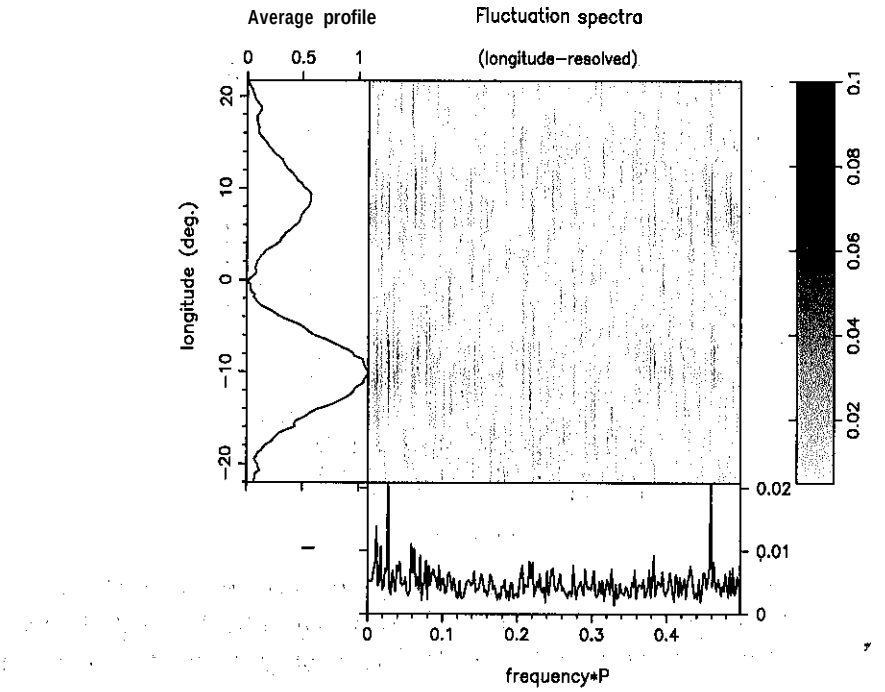

Figure 5.7: An lrf-spectrum of set-1 in the case of PSR0943+10 (over 512 pulses). The strong feature at $\bar{} 0.46\, c/P_1$ is related to the subpulse drift, while we relate the strong feature at $0.027\, c/P_1$ to the circulation time for this pulsar. Note the high Q-value of the two features.

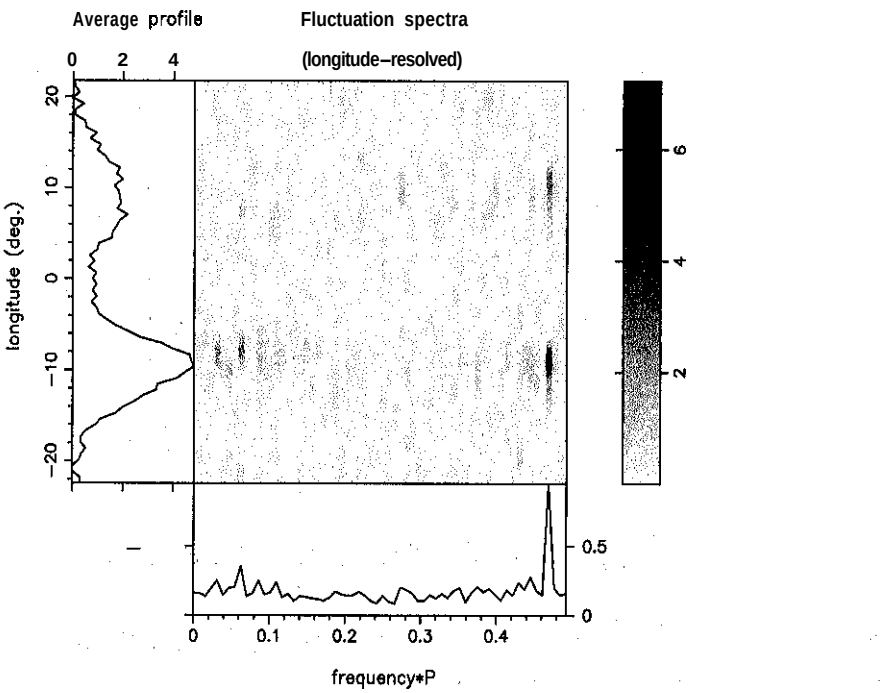

Figure 5.8: An lrf-spectrum of data set-2 over 128 pulses (B0943+10). The slower modulation feature, so prominent in the above figure, is not present here.

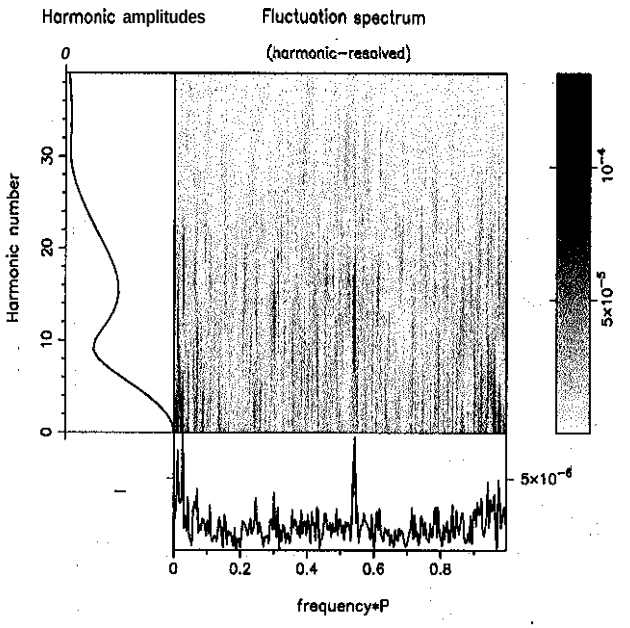

Figure 5.9: Hrf-spectrum of data set-1 of B0943+10. The asymmetry between the aliased components of the primary fluctuation (close to 0.5 c/P_1) is clear, which indicate? that the fluctuation is a phase modulation. The slower modulation (at $\sim 0.03\,c/P_1$) is also seen at its true frequency (see text more details).

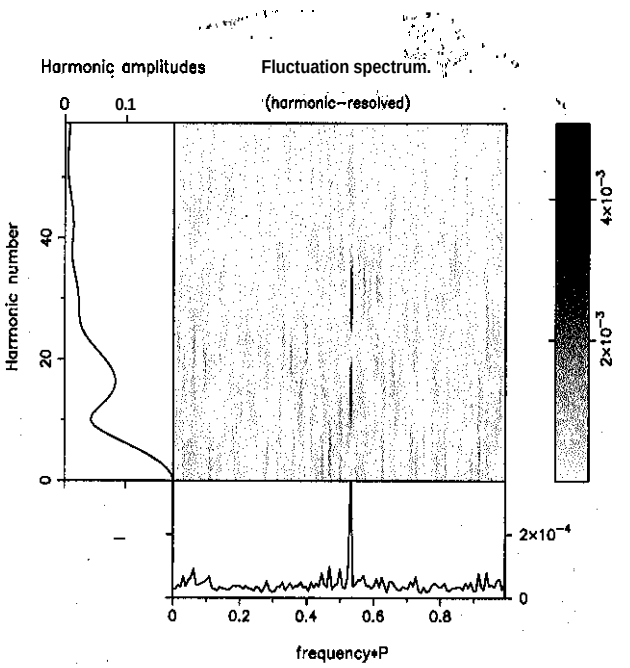

Figure 5.10: Hrf-spectrum of set-2 of B0943+10.

The drift bauds related to both the components are clearly visible and exhibit a phase difference between the modulation peaks. The "bridge" between the two components in the average profile displays little discernible fluctuation power, so we could be 'missing' one or more drift bands in this longitude range. We therefore express the modulation phase separation between the two component

(with the modulation phase going from positive to negative rotational longitudes) as,

$$\delta\zeta = 2\pi\,(X \pm m), \tag{5.29}$$

where, Awn set-2, X is -0.8 in the case of a negative drift, and +0.8 for a positive drift, with $m = 0, 1, 2, 3 \ldots$. The estimates agree even in the case of set-3, seen in figure 5.12.

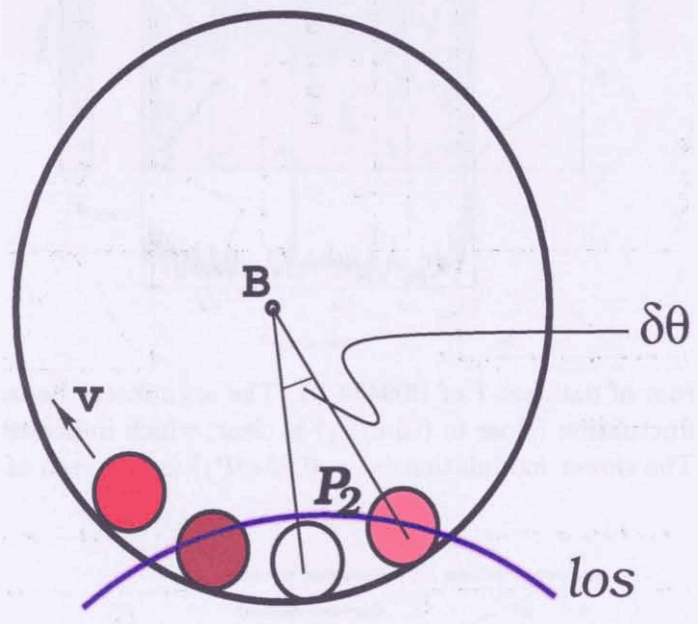

Figure 5.11: A cartoon of subpulse drift on the polar cap, as envisioned by Ruderman & Sutherland (1975). Here, '*los*' denotes the locus of the observer's sightline, B denotes the location of the magnetic axis (believed to be the center of the polar cap), v denotes the speed of the 'apparent' drift, 68 denotes the magnetic azimuth angle between two adjacent subbeams, and P_2 denotes the spacing of the drift bands.

Keeping in mind the picture advanced by Ruderman & Sutherland, we think on the following lines. If the modulation under the two components is caused by 'passage' of the same emission entity through our sightline as the emission pattern rotates around the magnetic axis (refer to the cartoon in figure 5.11), we can ask: For two points on the polar cap periphery (considered roughly circular from DRa) with a separation ($\delta\varphi$) of 20° in pulse longitude, what is the value of P_2 if the modulation phase difference (in P_3) between the two points ($\delta\zeta$) is as given in eq. 5.29? A longitude difference of φ is related to the distance on the polar cap as $68 = 2\,sin^{-1}\,[sin(\alpha + \beta)\,sin(\varphi/2)/\,|\,sin(\beta)\,|]$ (eq. 1.15, eq. 3 of paper-I). So, the angle subtended by the profile components at the magnetic pole is $\delta\theta = 34.3°$, where we use the values of α and β estimated in paper-I. We tabulate the values of P_2 and P_3 for the positive and negative drift in table 5.1.

In *figure* 5.12, the one full cycle of drift modulation under each component, as can be seen from the drift bands, suggests $P_2 \sim 12°$. For comparison, we can also use the peak of the modulation

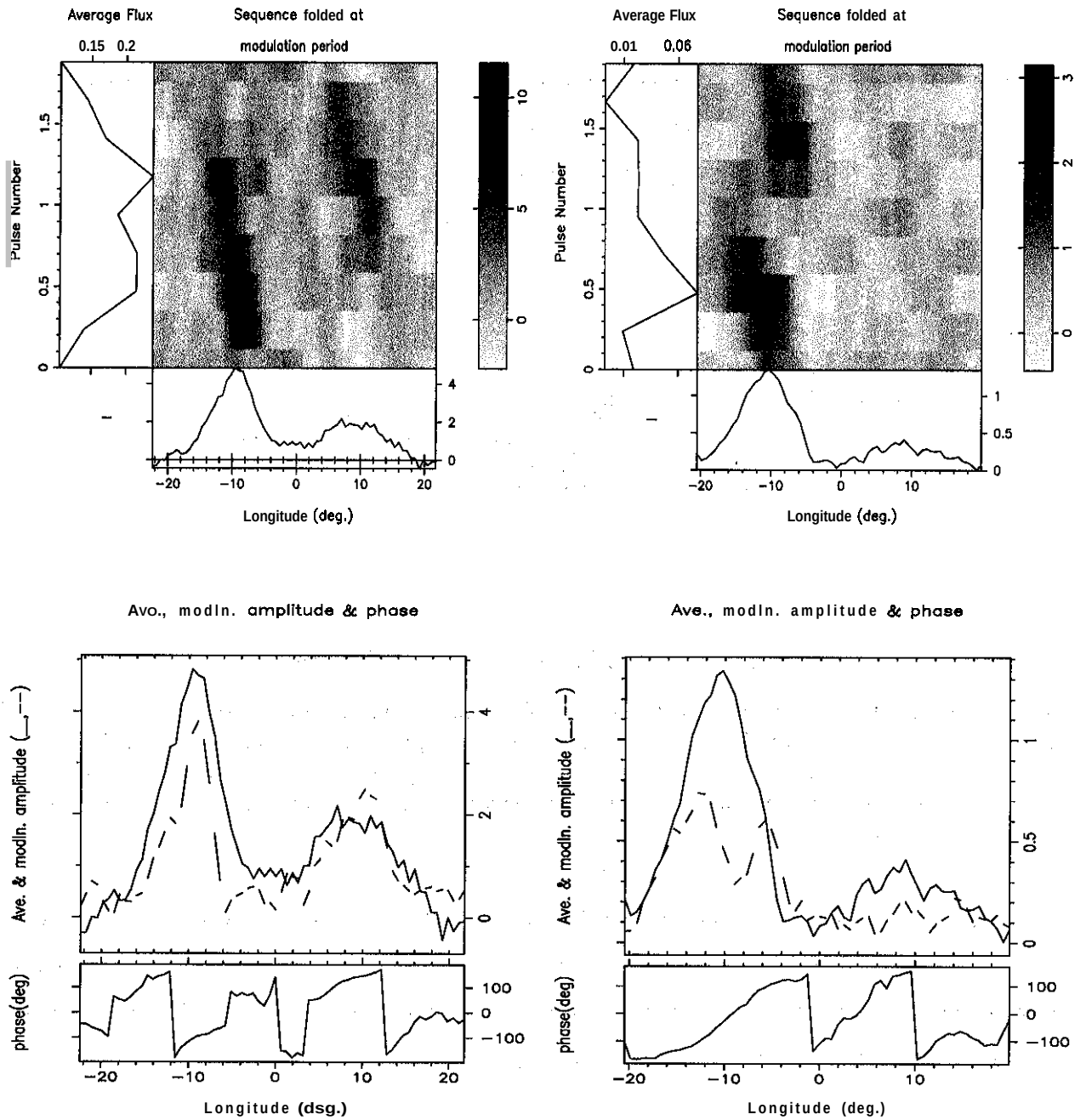

Figure 5.12: **Top:** The data sets 2 (left) and 3 (right) of B0934+10 folded at the corresponding primary fluctuation period P_3. The drift bands corresponding to two components are clearly seen, and so is the phase shift in the drift bands under the two components. **Bottom:** The average power and phase of the primary modulation plotted across the pulse longitude for set-2 of B0943+10 (left). A similar plot for set-3 is shown on the right. Notice that the phase of the modulation has a similar shape under both the components. The 'S'-curve of a drift modulation phase is clearly seen under the leading component and, is apparent even under the trailing component. Note that the phase estimates can be considered reliable only when the modulation amplitude is significant (compared to the noise level).

$X = +0.8,\ P_3 = 2.179\,P_1$	m	-2	-1	0	1	2
	$\hat{P}_3$ (error ± 1.5 P$_1$)	-27.4	-4.7	18.3	41.2	64
	P_2	7.4	1.2	5.0	11.1	17.2
$X = -0.8,\ P3 = 1.848\,P_1$	m	-2	-1	0	1	2
	$\hat{P}_3$ (error 1 . 5 P)	-54.3	-34.9	-15.6	3.9	23.3
	P_2	17.2	11.1	5	1.2	7.4

Table *5.1:* The estimated P_2 and $\hat{P}_3$ for B0943+10 corresponding to positive and negative drift, and different values of m & X. The negative sign for $\hat{P}_3$ in the table implies a negative drift (clockwise rotation around the magnetic axis). The error in $\hat{P}_3$ is estimated from the corresponding error in X *(10%).*

phase rate, which is the reciprocal of the subpulse drift rate (P_2/P_3), to estimate the P_2. Since the modulation in our data is not a pure phase modulation (drift is not entirely linear), this estimate yields an upper bound. From $d\zeta/d\varphi \geq 26°/°$, we get an upper bound on P_2 $(= 360°/d\zeta/d\varphi)$ as $\lesssim$ *13.6.* From table *5.1,* for negative or positive drift direction, for $|$ m $| = 1$, we have $P_2 \sim 11°$. It would imply that the profile components suhtend an angle of about twice the subbeam separation in magnetic longitude. Clearly, our line-of-sight crosses the hollow cone more centrally than at higher frequencies. For a P_2 of 11°, using eq. *1.15,* the magnetic azimuth separation between subbeams is estimated to be about 18°, suggesting a rotating system of about *20* subbeams.

It is clear from the above, that

- the *35-MHz* observations exhibit phase modulation very similar to that noted at higher frequencies.
- the true frequency of this modulation is $n + 0.541 \pm 0.00012\ c/P_1$, *i.e.* $P3 = 1.848 P_1$ when $n = 0$. The subpulse drift direction with respect to that of star's rotation is still ambiguous, which again makes the determination of the true frequency of the primary modulation ambiguous. We note that some enhancement in the spectral power is evident at $0.06\ c/P_1$, corresponding to the additionally aliased second harmonic of the primary modulation feature.
- The frequency and Q-value of the primary fluctuation feature are in excellent agreement with those based on the analysis of *430-MHz* observations,

The feature-2, at $0.0271 \pm 0.0018\, c/P_1$, is new and also has a high Q. Both the lrf-spectra and hrf-spectra display the feature at the same frequency. It is unlikely that such a feature is aliased multiply in our spectra, and we believe that $0.0271\, c/P_1$ is its true frequency. It is important to note that this feature, seen in set-1, is **not** apparent in the corresponding spectra of 111 and 430-MHz data (Paper-I), as well as our other data sets at 34.5 MHz. We discuss the significance of this feature below.

Amplitude modulation feature and the number of rotating subbeams

If indeed the observed drift was generated due to a steady rotation of a system of –20 subbeams around the magnetic axis, it should display a fluctuation feature in our fluctuation spectra of the period corresponding to the circulation time of about $\sim$ 40 P_1. We then look carefully at figure 5.7, and indeed find feature-2 at a frequency of $\sim 37 P_1$! A straight-forward calculation, $0.541/0.027 = 20$, shows that the features are harmonically related within their errors. We have looked for the sidebands (at $\pm 0.027\, c/P_1$) around the phase modulation feature at $0.541\, c/P_1$. Such side-bands were also identified in some parts of the 430-MHz sequence (see Paper-I and DRa), but they occur in our data at a much lower level of significance (see the central panel of figure 5.7). The feature-2, as did the 430-MHz side-bands, suggests a slower amplitude modulation, with a periodicity, $\hat{P}_3$, of some $37\, P_1$, or just 20 P_3.

These circumstances, along with the high Qs of the modulation features, imply a stable underlying circulating pattern of 20 subbeams, with the period of the low frequency feature (feature 2) providing a direct estimate of the circulation time of this pattern. This slow modulation may also be partially a phase modulation considering the asymmetry in the features at $0.027\, c/P_1$ and $0.973\, c/P_1$ (figure 5.9). This would imply some non-uniformity in the spacing of the subbeams.

From table 5.1, the value of the circulation time estimated above ($\sim 37 P_1$) agrees with the value corresponding to $m = -1$ and a negative drift, $P_3 = 1.848\, c/P_1$ ($\hat{P}_3 = 35 P_1$). This agreement seems to resolve the drift direction in this case. We further 'tune' our estimated parameters, and better resolve the drift direction using the closure in the forward and inverse of "Cartographic Transform". We elaborate on this more in section 5.3.2.

The circulation time of the polar pattern is $\hat{P}_3 = 36.96 P_1 \approx 40.6$s. Hereafter, while assembling the polar maps of emission, we make no use of the subbeam number n, once we have determined this value.

5.2.3 B0834+06

This pulsar displays a well-resolved double profile at frequencies ranging all the way from 35 MHz to 1 GHz. It shows frequent, short nulls, and is also known for its alternate pulse-intensity modulation. Gil, 1987, has reported the presence of strong OPMs in the case of this pulsar, where the individual polarization modes are completely polarized and are not distributed uniformly across the pulse window. We discuss our detailed analysis of two data sets from this pulsar at 35 MHz and estimate the circulation time.

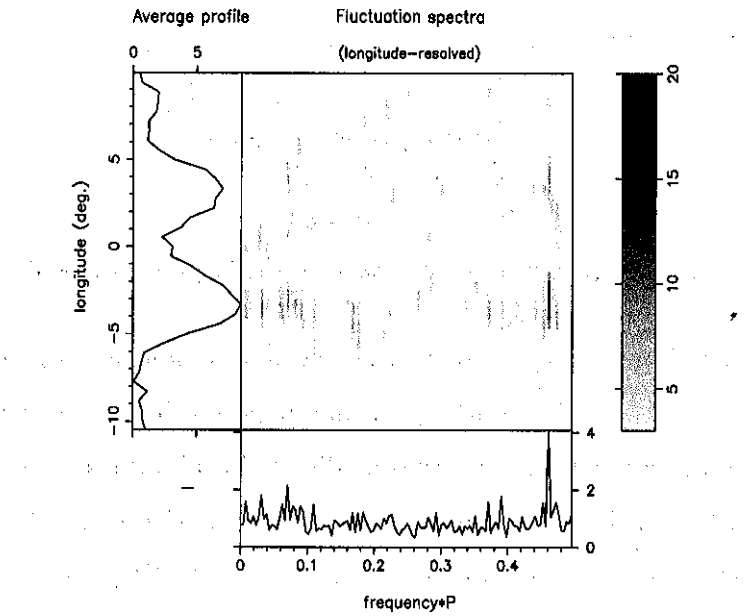

Figure 5.13: An lrf-spectrum for B0834+06 data set-1. The strong primary fluctuation feature appears barely resolved here, where we have used 256 pulses.

Spectra

The lrf-spectra for set-1 and set-2 of B0834+06 are shown in figures 5.13 and 5.14. Both spectra show a strong feature at $\sim 0.46\ c/P_1$ (hereafter referred as feature-1). The feature appears resolved in the spectrum (figure 5.13) constructed with a 256 pulse-transform, indicating a Q-value of $\approx$ 100. This feature refers to the alternate pulse-intensity modulation observed in this pulsar. The phenomenon causing the observed fluctuation is not as stable as observed in the case of B0943+10. The frequent, short, nulls (typically 1 or 2 null pulses over $\sim 10 - 20$ pulses) may further broaden its primary fluctuation feature, as was noted by Lyne & Ashworth (1983) in the case of another well studied drifter, B0809+74. Due to inadequate sensitivity, we can not even assess, leave alone account for, such a "contamination".

We look at the hrf-spectrum of this pulsar shown in figures 5.15 and 5.16 for the two sets.

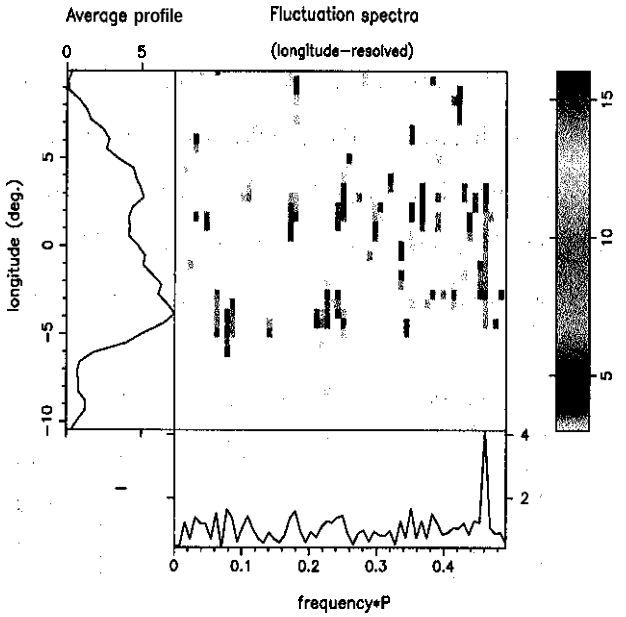

Figure 5.14: An lrf-spectrum constructed from 128 pulses of B0834+06, set-2.

The spectrum in figure 5.16 displays a pair of strong fluctuation peaks placed at $0.54\,c/P_1$ and $0.47\,c/P_1$. Such a pair of features in an hrf-spectrum represents the most general form of amplitude modulation in the data (section 4.2.2). There is no direct clue about the order of the aliasing of the primary modulation. In addition, in figure 5.15, we also find another pair of features at 0.463 ± 0.069 flanking the feature-1 (feature-1 has a frequency $0.463 \pm 0.001\,c/P_1$). In the figure, the side-tone close to $0.4\,c/P_1$ is clearly seen (a frequency of $0.390 \pm 0.001\,c/P_1$), whereas the other (upper side-tone) falls very close to the (aliased) symmetrically located component of the primary fluctuation feature. These features suggest the presence of a slower amplitude modulation on the primary fluctuation. The period of this slower modulation is $14.5 \pm 0.8\,P_1$, where the larger uncertainty is due in the estimation of frequency of the out-rider located near $0.53\,c/P_1$.

So, we observe a primary modulation (with a Q-value of 100-200), which is modulated by a slower fluctuation with a period of $14.5 \pm 0.8\,P_1$. Overall, this behavior is qualitatively very similar to the case of PSR0943+10.

Aliasing and the circulation time

We now fold the pulse sequence set-1 at the primary fluctuation period ($P3 = 1.856 P_1$), and examples for the pulse sequences in set-1 and set-2 are displayed in figure 5.17. The modulated intensity follows the average pulse shape of the pulsar. The phase of this modulatiou varies very slowly across the pulse (figure 5.17). The average phase rate is $3.8°/°$, consistent with its being an amplitude modulation. The folded sequence also shows a lag between the peaks of the drift pattern

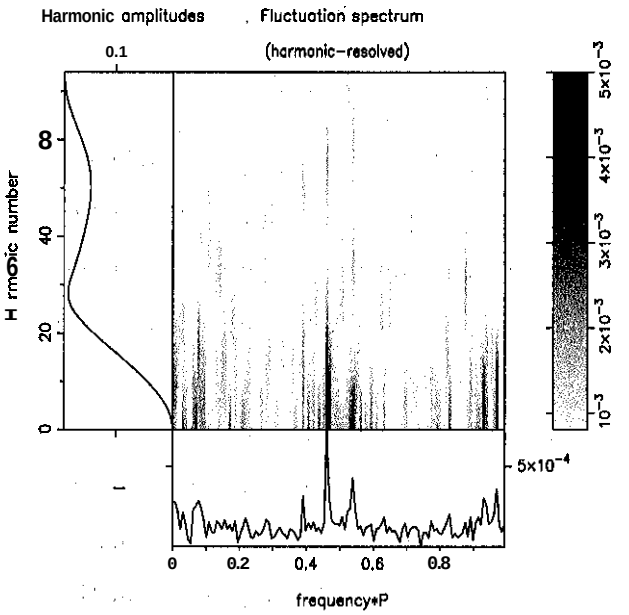

Figure 5.15: Hrf-spectrum for B0834+06 data set-1. A pair of features placed symmetrically around $0.5\,c/P_1$ are seen. Also seen are two sidebands on the primary fluctuation feature, which indicate the presence of a slower modulation in the data modulating the primary fluctuation (refer to text for details).

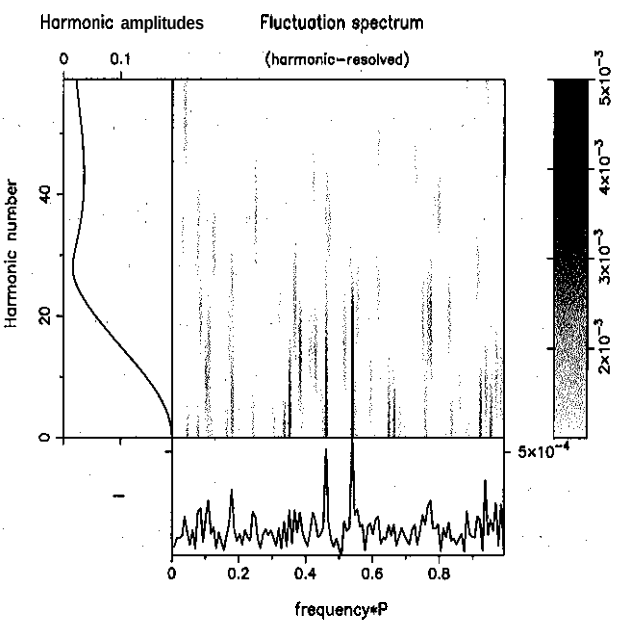

Figure 5.16: Hrf-spectrum for B0834+06, set-2.

under the two components in the average profile. Based on the difference of 24° in the modulation phase for the two components from the data set-1 for this pulsar (figure 5.17), the delay in the modulation corresponding to the two components can be expressed as

$$\delta\zeta = 2\pi\,(X \pm m) \tag{5.30}$$

where, X is -0.07 for a negative drift ($P_3 = 1.855\,P_1$) and +0.07 for a positive drift ($P3 = 2.164\,P_1$), with m $= 0, 1, 2, 3 \ldots$. From the data set-2 we estimate X $= \pm 0.11$ (figure 5.17).

The delay between the modulation under the two components in this case is interpreted, similar to the case of B0943+10, as caused by 'passage' of the same emission entity through our sightline as the emission pattern rotates around the magnetic axis (refer to the cartoon in figure 5.11). From eq. 1.15, a component separation of $\delta\varphi = 6°.2$ in rotational longitude implies a magnetic azimuth separation $\theta \simeq 56°$ around the magnetic axis of the star[2] (see figure 5.11). We can now directly estimate the circulation time of the pattern using the relative shift between the modulations as given by eq. 5.30. Assuming, following DRa, that the polar cap periphery is roughly circular, and using the component separation ($\delta\theta$) of 56° in azimuth around the magnetic axis, the value of the circulation time for different values of m is given by

$$\hat{P}_3 = \left(\frac{360°}{\delta\theta}\right)\frac{\delta\zeta}{2\pi}P_3 \tag{5.31}$$

$$= \left(\frac{360}{\delta\theta}\right)(X \pm m)\,P_3. \tag{5.32}$$

The estimates, corresponding to various values of m, are listed in the table 5.2.

If, indeed, the observed drift was generated by a steady rotation of a stable pattern around the magnetic axis, it should result in a fluctuation feature in the spectra of the period corresponding to the circulation time. The sidebands of the primary modulation noted earlier in 5.2.3, have a period of $14.5 \pm 0.8\,P_1$, close to the estimate corresponding to m=+1 in table 5.2. This agreement corresponding to a $P_3 = 2.164$ resolves the alias ambiguity, and suggests the drift to be positive (from leading component to the lagging component), corresponding to m = 1. The correlation map for this pulsar with a delay of 1 pulse period (section 4.3: figure 4.11) also indicates a positive drift. We also note that there is an excess of power at close to $13.7\,P_1$ (corresponding to a frequency of $0.073 \pm 0.007\,c/P_1$) in the lrf-spectrum of this data set (figure 5.13).

Hence, we would like to argue that we have indeed estimated the circulation time for the underlying polar emission pattern for this pulsar, $\hat{P}_3 \sim 14.8 P_1$. The direction of the drift, with or

[2]We have used $\alpha = 30°$ and $\beta = -3°$ in the above estimation. The value of α as well as the sign of β is uncertain. However, the magnitudes of α and β are consistent with the PA-sweep rate reported by Stinebring *et al.*,1984.

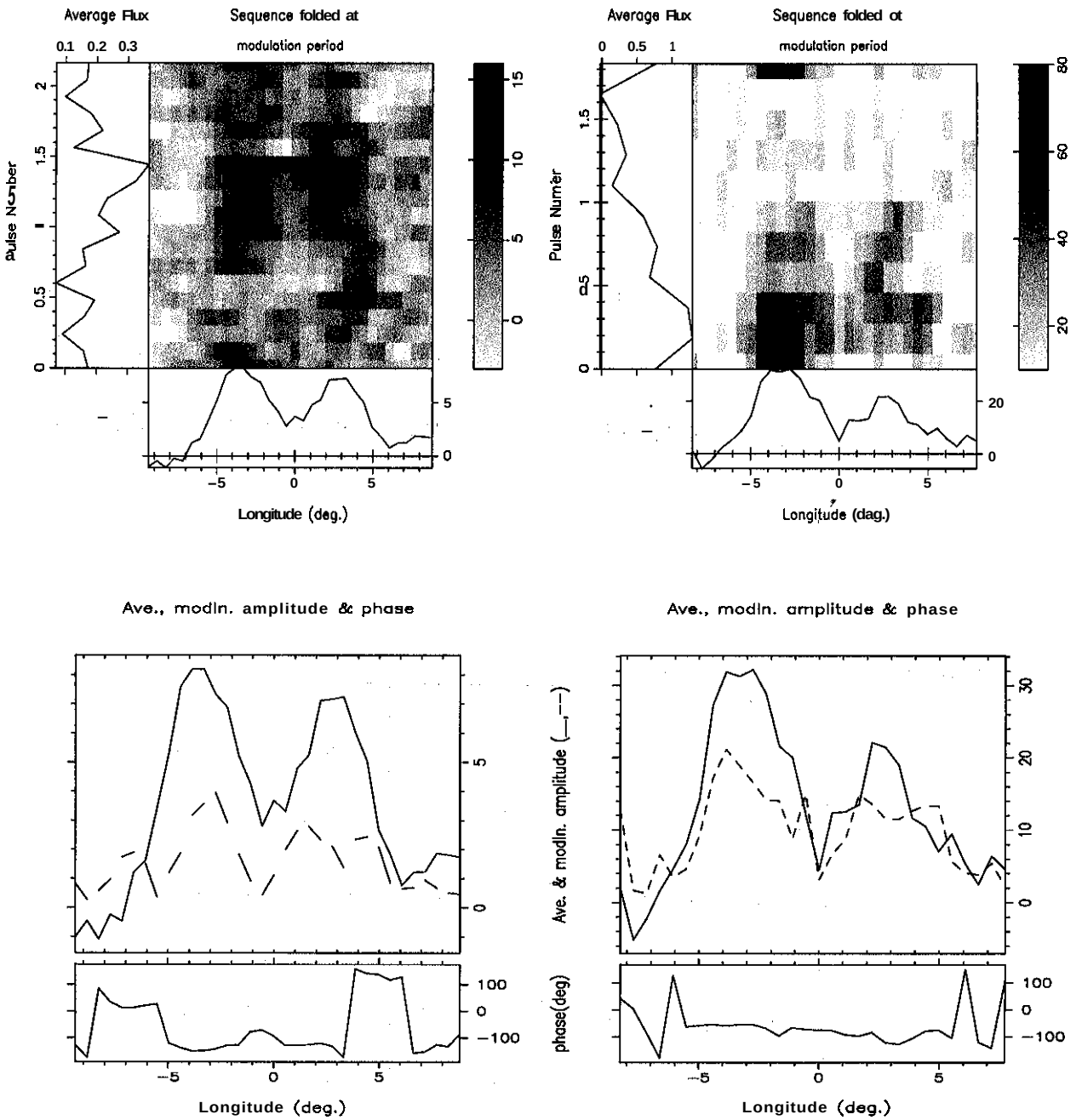

Figure 5.17: **TOP:** B0834+06 data set-1 (left), and also set-2 (right), folded at the corresponding primary fluctuation period P_3. The delay in the modulation under the two components is evident. **BOTTOM:** The average power and phase of the primary modulation plotted across the pulse longitude set-1 of B0834+06 (left). A similar plot for set-2 is shown on the lower right. Notice that the phase of the modulation has similar shape under both the components and varies slowly across the pulse, consistent with an amplitude modulation.

Set-1 (X=0.07)

m	-2	-1	0	1	2
$P_3 = 2.164\,P_1$ (error in $\hat{P}_3 = 0.1P_1$)	26.8	12.9	1.05	14.9	28.8
$P_3 = 1.855\,P_1$ (error in $\hat{P}_3 = 0.1P_1$)	23.0	11.1	0.8	12.8	24.7

Set-2 (X = 0.12)

m	-2	-1	0	1	2
$P_3 = 2.164\,P_1$ (error in $\hat{P}_3 = 0.25P_1$)	-26.1	-12.2	1.7	15.6	29.5
$P_3 = 1.855\,P_1$ (error in $\hat{P}_3 = 0.25P_1$)	-25.2	13.3	-1.4	10.5	22.4

Table 5.2: The estimated circulation time corresponding to different values of X, P_3 and m from the two data sets of B0834+06. Errors in such an estimation are also mentioned.

against the pulsar rotation, is ambiguous, an issue related to the uncertainty in the sign of β, even though we may have resolved the aliasing of the primary modulation feature in the lrf-spectrum.

The derived estimate depends on the pulsar geometry, and we note that the present polarization data for this pulsar do not constrain the viewing geometry, especially the sign of β effectively. We further 'tune' the parameters, and resolve the drift direction, by using the closure in the forward and inverse of "Cartographic Transform". We elaborate on this more in section **5.3.2,** where we discuss the uniqueness of the polar maps derived from this procedure.

5.3 Cartographic transforms

If the polar emission pattern responsible for the observed fluctuations is stable over multiples of its circulation time around the magnetic axis, then we can study the entire emission region using a suitably large number of pulses, which will sample the emission region on the average completely and uniformly. We can, thus, transform the pulse sequence from the observer's frame (as a function of the rotational longitude) to the frame of reference rotating around the magnetic axis with a period of $\hat{P}_3$.

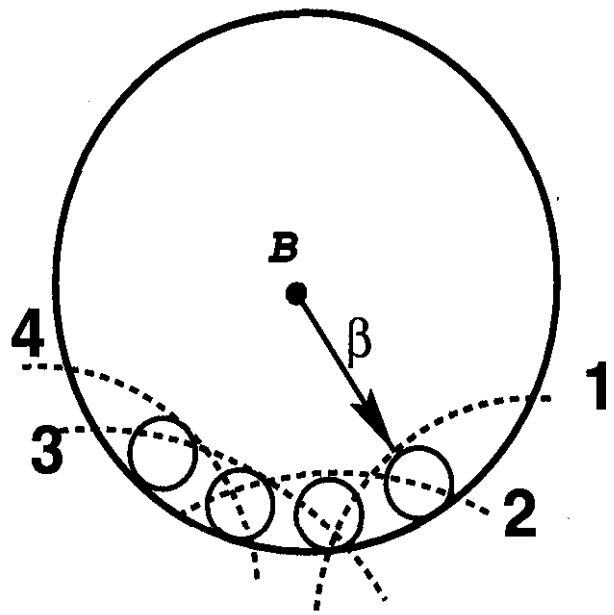

Figure 5.18: Cartoon of the polar emission pattern being sampled by a single-pulse sequence. The magnetic axis, denoted by B, is at the center of emission region, and the loci of successive pulses are denoted by the respective pulse numbers. In each pulse the closest approach of the observer's sightline to the magnetic axis is given by β.

If we knew the geometry of our viewing of the pulsar emission cone, this "Cartographic Transform" will then map the intensity as a function of longitude (with respect to that of the rotation axis) $\varphi - \varphi_0$ and pulse number $k - k_0$ into magnetic-polar colatitude R and azimuth θ (round-trip period of $\hat{P}_3$). In successive pulses (after a duration of P_1 each), our line-of-sight samples the intensity along different quasi-chord-like traverses (corresponding to different azimuth intervals) through the rotating polar emission pattern. This is depicted in the cartoon shown in figure 5.18.

5.3.1 Details of equations

We wish to detail here (following the notation adopted by Deshpande & Rankin (2001) — paper-I) a coordinate transformation between the usual system of pulsar (rotational) colatitude ζ (= a + β) and longitude φ and a system rotating around the magnetic axis described by colatitude R and azimuth O. The emission beams rotate around the magnetic axis with a period $\hat{P}_3 = n P_3$, where n is the number of subbeams and P3 the usual subpulse-drift interval.

We number the pulses by k from a reference pulse k_0 and measure the longitude φ relative to an origin defined by the longitude of the magnetic axis φ_0, then Θ is the sum of a rotation θ_{rot} and a transformation θ_{trans} as follows

$$\Theta = A\,\theta_{rot} + B\,\theta_{trans}, \tag{5.33}$$

where A and B take a value either +1 or −1. The sign of θ_{rot} (value of A) will be equal to to the sign of the observed PA sweep rate. This, in the case of B0943+10 is negative and is in accordance with the Ferraro's theorem (see Ferraro & Plumpton, 1966). The sign of θ_{trans} (*i.e.* B) is positive for cw rotation (of the rotational pole which is closest to the sight line) and negative for ccw rotation. Then,

$$\theta_{rot} = [k - k_0 + (\varphi - \varphi_0)/2\pi]/\hat{P}_3, \tag{5.34}$$

$$\theta_{trans} = sin^{-1}\left\{\frac{sin(\alpha+\beta)\ sin(\varphi-\varphi_0)}{sinR}\right\}, \tag{5.35}$$

where,

$$\mathrm{R} = 2\,sin^{-1}\left\{sin^2((\varphi-\varphi_0)/2)sin\alpha\ sin(\alpha+\beta) + sin^2(\beta/2)\right\}^{1/2}. \tag{5.36}$$

It is possible that the rotation of the subbeam pattern is not a rigid rotation, but the period has a dependence on the angular distance from the magnetic axis. We model the possible $\hat{P}_3$ dependence on R as follows

$$\hat{P}_3(R) = \hat{P}_3(\beta)\,[R/\beta]^{\delta_R}, \tag{5.37}$$

where δ_R is, in general, a real number. However, in these cases the apparent constancy of P_3 across the pulse window of the pulsars suggests that, at least over the narrow-cone thickness the rotation is near-rigid, *i.e.* $\delta_R = 0$, a provisional value that we will assume.

The estimation of rotational longitude of the magnetic axis, φ_0, is very important. The profiles for B0943+10 at 430 MHz are highly asymmetric, narrow, and when compared in a series of time-aligned average profiles from a multi-frequency data, appears to peak at an earlier longitude.

DRa resort to elaborate profile matching to obtain an initial estimate of φ_0. In our case, the B0943+10 profile is a well separated "double". The longitude φ_0 can be clearly defined as the 'center' of the profile, the so called fiducial point. The average pulse energy and fluctuating power was found to drop to zero at the center. Hence, this definition is less uncertain in our case. For B0834+06 we do not have such determination of the zero-longitude. We fit the profile for two Gaussian components and estimate the magnetic longitude as associated with the location midway between the two peaks.

5.3.2 Tuning : consistency check for the parameters defining the transforms

We now ask the obvious question: How unique or accurate are the results given by the mapping technique involving a "Cartographic Transformation" ?

The correctness of the transform (and uniqueness of the maps of emission) depends only, and directly, on the correctness of the emission geometry and the drift parameters which are required to carry out the transform. It is very sensitive to the circulation time $(\hat{P}_3')$, the longitude of the magnetic axis (φ_0), and the sense of the sightline traverse, $(i.e.$ the sign of $\beta)$. If these estimates are incorrect the image will be smeared or distorted. Any error in the value of a, however, largely just scales the image, so that its correct specification is much less crucial, as long as the ratio of $sin(\alpha)/sin(\beta)$ is unchanged.

However, the forward transform used to construct the maps has a unique inverse transform. The maps reconstructed from observed data can be an input to this inverse transform, which would then produce an artificial pulse sequence, so called 'replayed sequence'. If the parameters used in the mapping transformation are indeed correct, then this replayed sequence should match the original (observed) one in its detailed fluctuation behavior. Comparison of the sequences is best effected on a longitude-to-longitude basis, such that the fluctuations in the new sequence at a given longitude are compared with those in the original one pulse-for-pulse and sample-for-sample. A simple cross-correlation coefficient, appropriately normalized, provides an adequate measure for such a comparison. The correlation coefficient defined over a range of longitudes must be combined through a suitably weighted average. Such a coefficient is a robust measure, for the two pulse sequences could differ by many conceivable ways $(e.g.,$ in average profiles).

The inverse transform thus provides a powerful "closure path" to verify, and even refine, the crucial parameter inputs related to the emission geometry. The inverse transform is, of course, defined by the same set of eq. (5.35 and 5.36) as for the (forward) "Cartographic Transform". In what is following, we demonstrate the use of this closure path in the case of B0943+10 and

B0834+06.

The power of this method is due to the averaging over the large number of pulses used to map the polar emission region (See Deshpande, 2000, for a detailed discussion on the issue). It is most sensitive to the circulation time, the ratio of the angles β and α, and the drift direction. The sensitivity to the values of these angles reduces for high values of α. The estimates of the viewing geometry using the polarization data are poor in such a situation as well.

5.3.3 Viewing Geometry of B0943+10

Being a steady "drifter", this pulsar is a member of S_d-class. The low frequency, time-aligned profiles show the expected profile bifurcation and an increase in component separation. Our sightline is highly tangential to the emission cone at 430 MHz ($\beta/\rho = 1.01$, from paper-I).

Deshpande & Rankin (Paper-I) have studied the emission geometry of B0943+10 most comprehensively. They used time-aligned average profiles over a broad frequency range, along with the full polarimetric data at 430 MHz. The specific points they dealt with are the following. Is it an inner or outer cone responsible for emission (Rankin, 1993)? Does our line-of-sight pass between the rotation and magnetic axes or outside this zone? Can we understand the pulsar's steep spectrum in terms of the frequency dependence of conal beam? And finally, can the observed subpulse separation in longitude be reconciled with the 20 subbeam pattern dictated by the fluctuation properties?

From all the available constraints, the model that best fits the data has

$$\alpha = 11°.64 \tag{5.38}$$

$$\beta = -4°.31 \tag{5.39}$$

and the inner cone as responsible for emission. In our reference frame the drift direction is in the same as the star's rotation. The subbeams rotate in the same direction relative to us around the magnetic pole, they rotate around the magnetic pole counter-clockwise (in the reference frame of the rotating star).

Here, we seek to demonstrate the usefulness of the closure technique, discussed in the section 5.3.2, for our data set-1. We have shown in figure 5.19 the auto-correlation of the actual sequence and its cross-correlation with the replayed sequence created using the correct parameters of the "Cartographic Transform". As a simple example, we discuss a model geometry differing only in the sign of β, and figure 5.20 displays cross-correlation of the replayed sequence with the actual one for such a case. In the another example, we chose a model geometry that is the same as the correct one but with the circulation period $\hat{P}_3$ slightly different (figure 5.20). In both the

cases, where we use the parameters of the transform different from the estimated 'correct' values, the cross-correlation coefficient between the replayed and actual pulse sequences (see section **5.3.2)** falls.' The cross-correlation in the off-diagonal region also shows deviations from the behavior observed in the case of the original data set.

5.3.4 Viewing Geometry of B0834+06

This pulsar is a member of the "D"-class, according to the Rankin classification. The emission is believed to come from the inner conal ring, and the geometrical parameters were derived accordingly. The two components in its profile are not fully resolved even at decameter wavelengths. This suggests a sightline traverse that is more central.

We carry over our discussion from section **5.2.3,** where we derived the circulation time from the fluctuation spectra. We now need to resolve the issue of the drift direction, and further "tune" our estimate of the circulation time.

The inverse of the "Cartographic Transform" is used to reconfirm our parameters. To achieve this, we carried out a grid search, where we chose the range of parameters used in the transform. We searched for α close to 30°, $-4.0 \leq \beta \leq 4.0$, the PA-sweep being positive or negative, if the drift direction is same to that of rotation, and $\hat{P}_3$ ranging from **5** to **40** P_1. The inverse of the "Cartographic Transform" is used to simulate a pulse sequence from a given polar emission pattern with a given set of parameters. In each step of the search, we estimate an average polar map from the observed pulse sequence. This polar map is then used as an input to create a simulated ('replayed') pulse sequence. We now cross-correlate the fluctuation properties of this replayed sequence with those of the original (observed) pulse sequence. The match was considered better for a higher average correlation.

As discussed in section **5.3.2,** this 'closure technique' involving the inverse transform is rather insensitive to changes in the values of α and β (α being larger in the case of B0834+06 as compared to B0943+10), and the sign of β was not constrained. The search is sensitive to the circulation time and the drift direction, and does allow us to constrain these parameters. This, in a way, also means that our results of polar emission maps are rather insensitive to errors in estimation of some of these parameters (*i.e.* α and β). We, in what follows, use the following set of refined parameters,

$$\hat{P}_3 = 14.84 P_1; \tag{5.40}$$

$$\alpha = 30°; \tag{5.41}$$

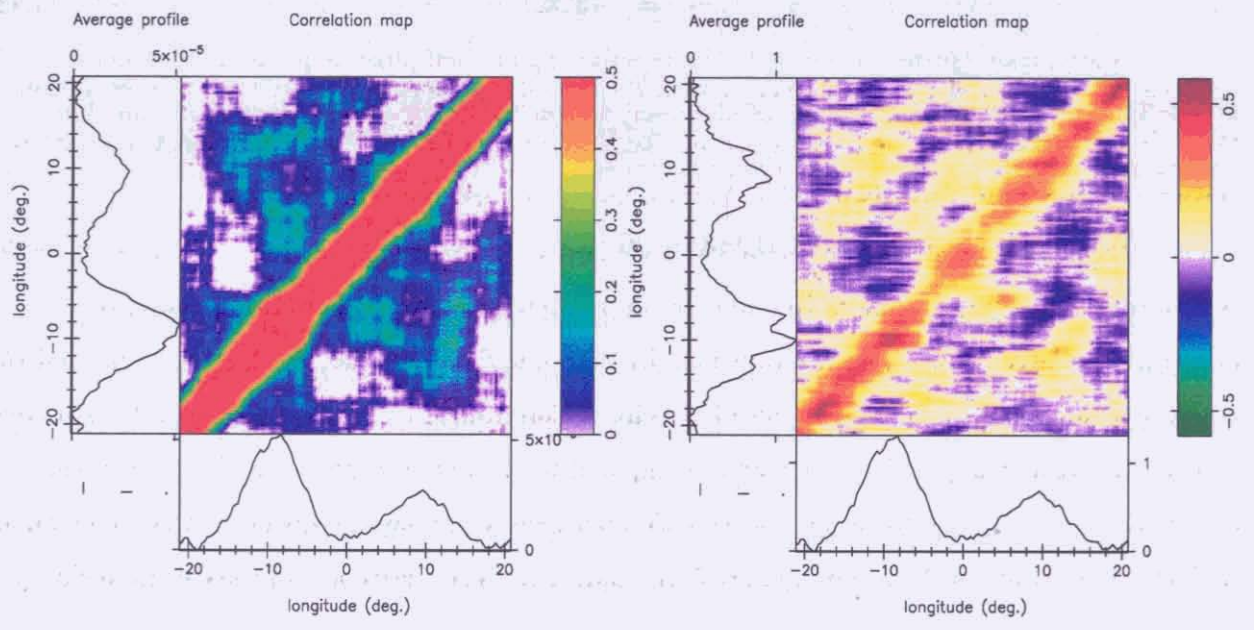

Figure 5.19: **B0943+10** : The auto-correlation of the observed pulse sequence in set-1 is plotted on the left. The cross-correlation between the 'replayed' data set, generated using the correct estimates of the parameters of the transform, is plotted on the right (see section 5.3.2 for details). The average cross-correlation coefficient along the diagonal is close to unity and any significant deviation is considered as an indication of a mismatch of parameters.

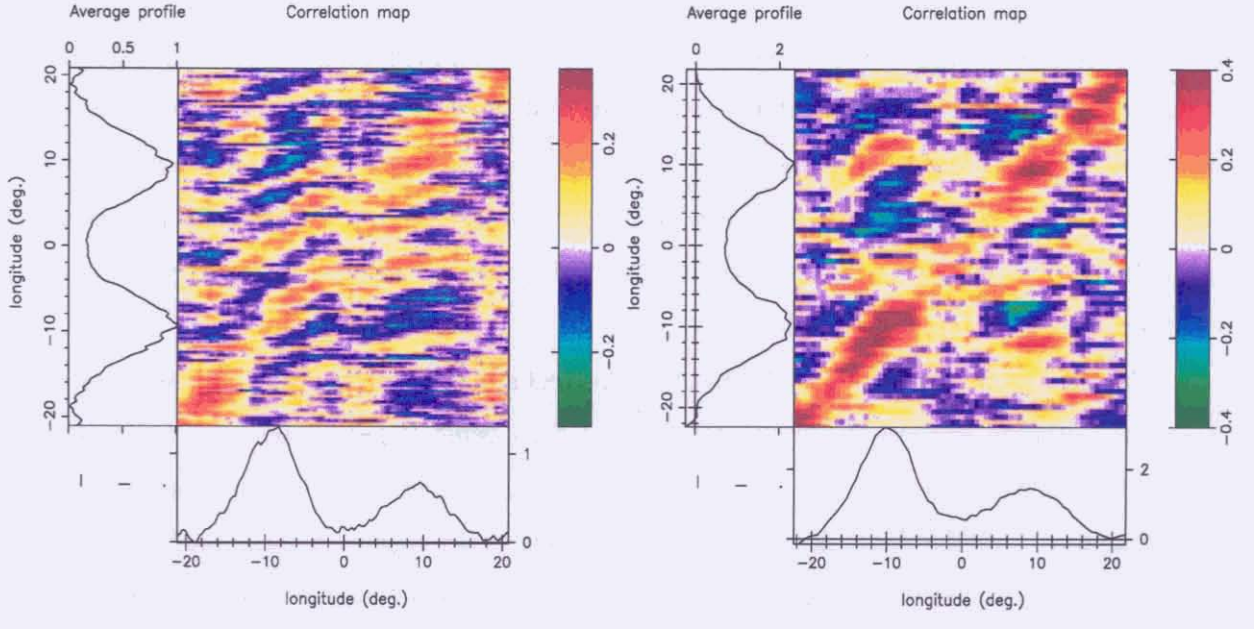

Figure 5.20: **B0943+10** : Plotted in the figure on the left is the cross-correlation between the actual pulse sequence and the 'replayed' sequence, where the latter was generated with the sign of β changed. A similar plot, where the 'replayed' sequence was generated with a $\hat{P}_3$ differing by $\leq 1.0\%$ from its estimated value, is shown on the right. In both the cases, the average cross-correlation along the diagonal has dropped compared to the corresponding plots in the top figure and the off-diagonal part shows significant deviation.

$$\beta = -3^{\circ}.0. \tag{5.42}$$

with the drift direction being same as that of the pulsar rotation. We note, that the resolution of the drift direction is also tied to the ambiguity in the sign of β and a comparison with Ferraro's theorem (Ruderman, 1976) is possible after an unambiguous determination of β.

Here we demonstrate the use of 'closure' checks in the case of this pulsar. We, for example, compare two model geometries. In one case, on the left in figure 5.22, we have changed the sign of the drift relative to the pulsar's rotation. In the same figure on the right, we have plotted the result of a similar analysis with a value of the circulation time differing by $\sim 1\%$ from its estimated value. The significantly different behavior compared to the actual correlation observed in the real data with zero-delay, and to the cross-correlation between the replayed sequence with correct values with the actual one (both shown in figure 5.21), indicates the effectiveness of the closure technique.

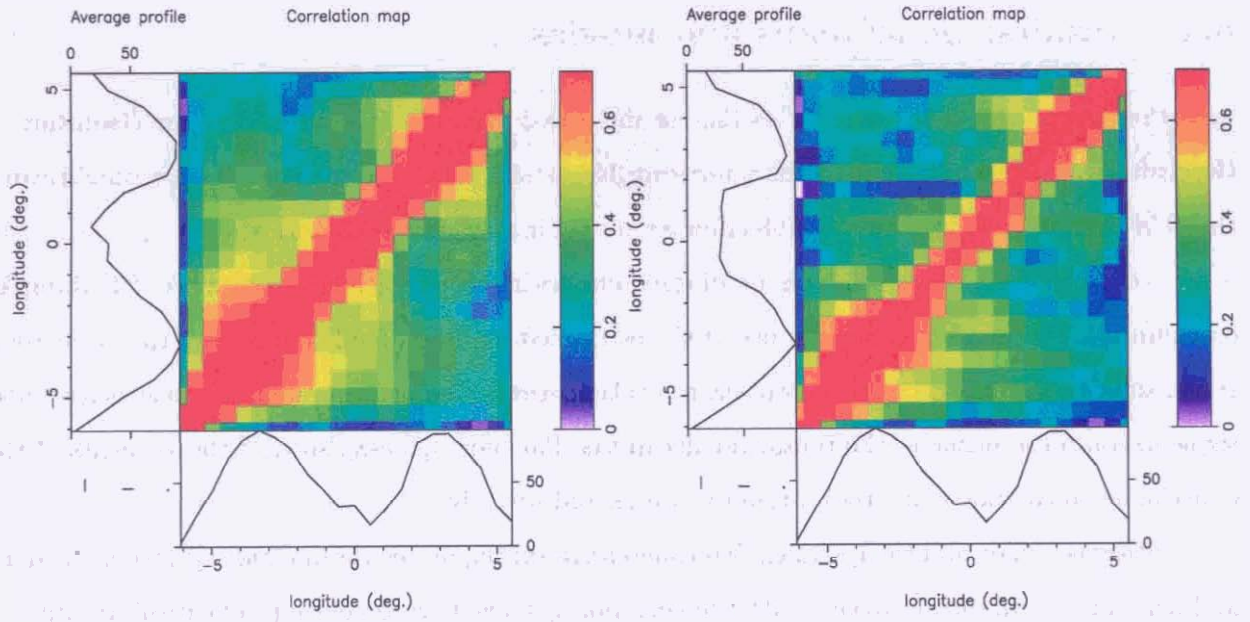

Figure 5.21: **B0834+06:** The auto-correlation of the observed pulse sequence in set-1 is plotted on the left. The cross-correlation between the 'replayed' data set, generated using the correct estimates of the parameters of the transform, is plotted on the right (see section 5.3.2 for details). The average cross-correlation coefficient along the diagonal is close to unity and any significant deviation is considered as an indication of a mismatch of parameters. The figure on the right displays all the essential characteristics of the autocorrelation of the actual data, the enhanced correlation close to the two components along the diagonal, slight correlation in off-diagonal areas, etc.

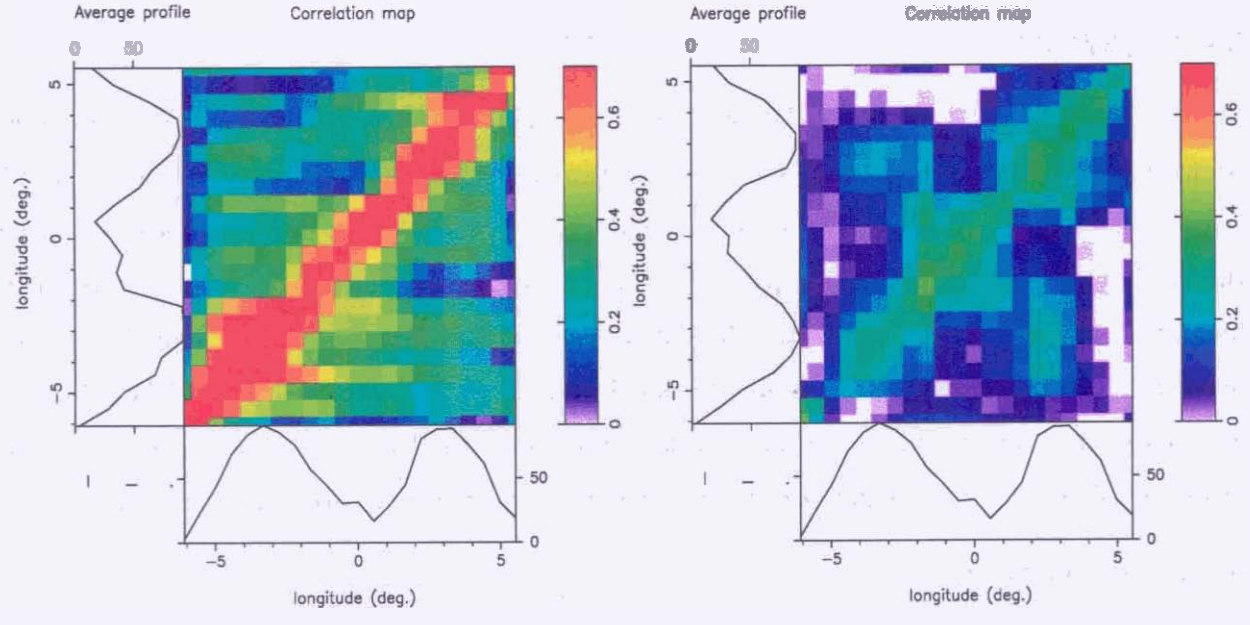

Figure 5.22: **B0834+06:** We have changed the sign of the drift direction (from + to -) with respect to the pulsar rotation, and have plotted the cross-correlation between the replayed sequence and the actual one (see the text for details). The average correlation in the diagonal region falls by 2%, compared to the plot above on the right. The correlation away from the diagonal has also reduced noticeably. A similar plot, where the 'replayed' sequence was generated with a $\hat{P}_3$ differing by $\leq 1.0\%$ from its estimated value, is shown on the right. There again the average cross-correlation along the diagonal has dropped by 40% compared to the plot in the top, right figure. The color scale of all the plots in these figures are adjusted to highlight details.

5.4 Results: polar maps and movies

In the last section, we discussed the technique and certain details of the "Cartographic Transform". Here we present the polar emission patterns at 34.5 MHz. The patterns were reconstructed using the "Cartographic Transformation" technique described in Section 5.3 with the viewing geometry of estimated in the paper-I, but taking all the values of $\hat{P}_3$ from our analysis of 34.5-MHz data. In assembling these maps we make no use of the estimated number of subbeams once the circulation time has been determined directly; rather, the "Cartographic Transformation" transforms the pulse sequence onto the frame of the pulsar polar cap [see Paper-I: eqs. 5-81, so that the elements of the emitting pattern and their distribution can be viewed directly.

Further, a series of maps, each from successive subsequences (of duration $\geq \hat{P}_3$) of the data and with a large fractional overlap with the neighboring ones, were generated. The resultant images were viewed in a slow 'movie'-like fashion, which allowed us to examine the change in the polar subbeam emission pattern with time. Since each of the images in a movie uses a relatively small number of pulses, the overall sampling of the polar region may be very patchy. We, hence, smooth the images suitably while ensuring that the basic details are not lost. Although the signal-to-noise ratio in one individual frame is poorer, certain significant characteristics of emission can still be ascertained.

5.4.1 B0943+10

We have six data sets from this pulsar wherein a clear detection was made. For three of these we could study single-pulse sequence and in these all cases we made polar maps and movies. While some features in the maps of B0943+10 were stable over only a few circulation times most, (*e.g.* the bright subbeams of the set-1 sequence in figure 5.23), remain relatively prominent *over* many hundreds of pulse periods. For all the three data sets discussed, in a set of successive frames of a movie a few subbeams usually dominate others in intensity. Overall, the brightness of the subbeams was observed to fluctuate by up to about a factor of 4 over the length of the sequence. Common properties shared by these sequences are accompanied by a few peculiarities, which we discuss now.

set-1 (13^{th} February 1999)

The fluctuation analysis of this sequence using 512 pulses has allowed us to determine $\hat{P}_3$ for this pulsar very reliably. The primary fluctuation feature (figure 5.7) has a higher Q-value of $\gtrsim 500$ compared to that in other pulse sequences. However, the overall modulation is rather weak (see figure 5.8 for a comparison). Figure 5.23 shows the average emission pattern mapped using 512

pulses from this sequence. Remarkably, the 'active' subbeams seem to occupy only about half of the conal periphery. Such a deep, systematic and smooth variation in the subbeam intensity around the emission cone is completely consistent with the appearance of the slow modulation feature in the fluctuation spectra (see figures 5.7 and 5.8). In this sequence, a few subbeams are persistently bright, accounting for most of the power in the average profile.

Set-2 (7^{th} February 1999)

In contrast to set-1, the polar image for this set, shown in figure 5.24, exhibits most of the 20 subbeams with a more-or-less uniform spacing and an unsystematic pattern of intensities—a picture which is also entirely compatible with the observed absence of any significant slow modulation feature in its fluctuation spectra (figure 5.8). It is worth mentioning that the power associated with the primary modulation (*i.e.* drift) is significantly higher in set-2 than in the set-1.

A very different behavior is seen from 'movies' of polar images constructed from the subsets of this sequence. Here the subbeams are all very weak and unstable in the initial part of the sequence. Then, they gradually increase in intensity until most of the 20 subbeams constitute a more-or-less stable configuration—that depicted in figure 5.24—for some four or five circulation times, whereupon they again gradually fade back into a disorganized pattern. The phase modulation feature is not readily detectable in either the pre- or post-bright phases. Neither, interestingly, are associated changes observed in the shape of the average profile; rather, it maintains a clear 'B'-mode profile form, apart from the changes in the average intensity.

Set-3 (12^{th} February **1999**)

In this B-mode sequence, the second component is considerably weaker than that in the earlier two sets. The data show some non-zero fluctuations even under this component. The primary modulation frequency matches with that in the earlier sequences, and so does the behavior of the phase of this modulation across the pulse longitude. We proceed to make the polar map using the circulation time derived earlier. A pattern of distinct subbeams appears only over a part of the sequence (see the polar map made over this pulse range, figure 5.25). The pulsed energy falls there-after considerably, and the corresponding average polar map shows deviation from the distinct subbeam pattern, whereas the pulsed energy is undetectable beyond $\sim$ 300 more pulse periods.

When viewed in a movie fashion, the overall polar pattern appears unstable, with the brightness of individual subbeams fluctuating wildly. From being very bright in certain frames, the subbeams even tend to be undetectable over certain other frames of the movie. The positions of

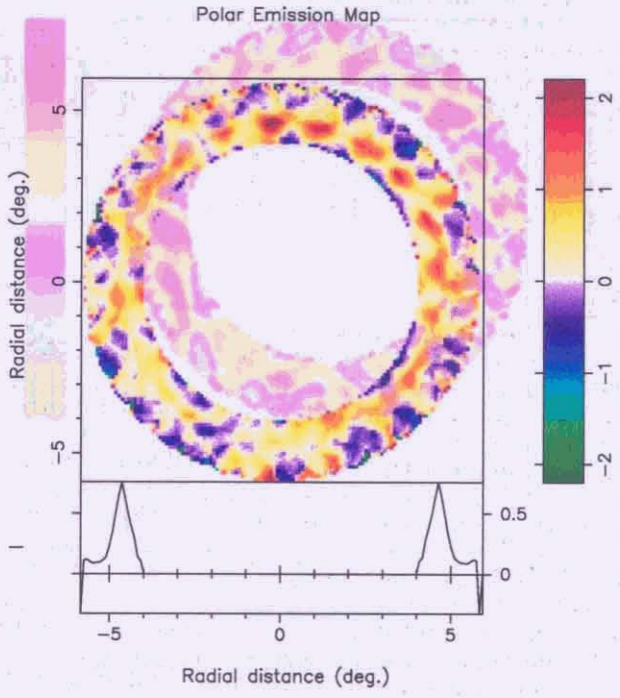

Figure 5.23: Average polar map of emission for B0943+10 set-1 made using 512 pulses. Note the remarkable asymmetry between the two halves of the polar cap, that gives rise to the slower fluctuation feature in the lrf-spectrum for this data set (see text for details).

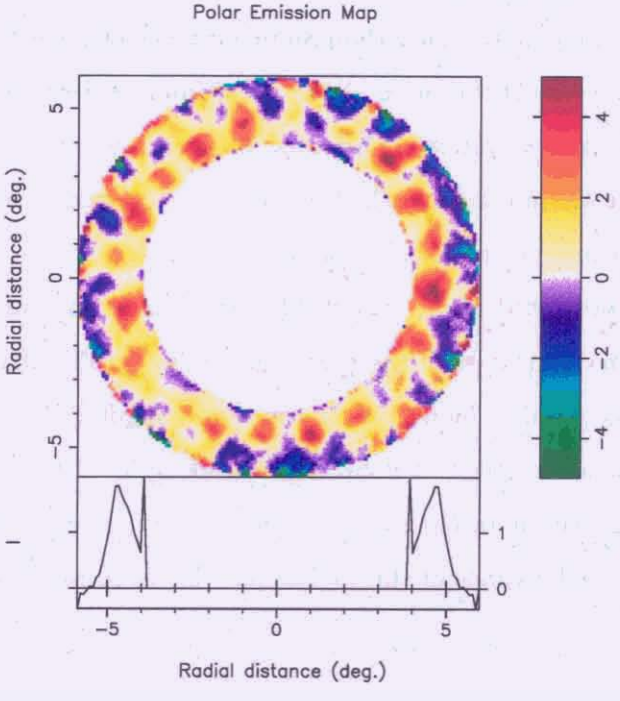

Figure 524: Average polar *map* of emission for B0943+10 set-2 using $\sim$ 125 pulses. Most of the subbeams are active, and there is no apparent modulation in their brightness. The average fluctuation power is found to be significantly *higher* than set-1.

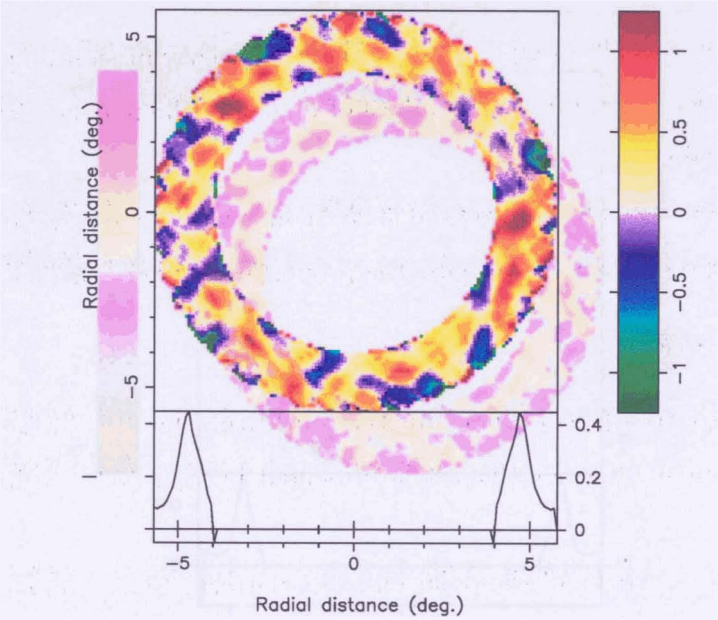

Figure 5.25: Average polar map of emission for B0943+10 set-3 using ~ 200 pulses from the middle of the sequence.

strong subbeams, however, appear to be stable over about 5 circulation times, which would then translate into the observed stable primary fluctuation. The average polar map would then appear as a "sum" of all individual polar maps from successive sub-sequences, with the appearance in one polar map not being entirely the same as the other intermediate ones. Such a situation is far removed from the 430-MHz observations. Moreover, a movie made from this pulse sequence shows bright streak patterns on the polar cap, which indicate some features on the polar cap that exist over time scales of about one pulsar rotation period or shorter.

In all the maps presented above, the radial sampling of the subbeams appears complete. This is significantly so in contrast with the partial sampling at 430 MHz. The situation is easily understood in terms of the possible increase in the apparent angular dimension of the emission cone, allowing a relatively central sampling at decameter wavelengths (RFM). The slight elongation (in the azimuth direction) apparent in the subbeam shape may not be real, but simply result from possible slight jitters in the locations of the subbeams relative to their average position.

5.4.2 B0834+06

We use the circulation time from eq. 5.42 to derive the polar emission maps of this pulsar. The maps are not very sensitive to the actual values of α and β, though the viewing geometry of the pulsar remains uncertain.

Out of the five available data sets at 34.5 MHz, two data sets were chosen for mapping. Here, we present our polar maps and discuss the properties of the polar emission pattern.

Set-1 (6^{th} February 1999)

This data set shows the sharpest primary fluctuation feature for this pulsar in our data, with a Q-value $\gtrsim 100$. The polar map for this set is presented in figure 5.26, which consists of bright, distinct subbeams.

We also viewed a 'movie' of the polar emission pattern. Since a polar map over one circulation time doesn't sample the polar cap of 8 subbeams adequately, in each frame of this movie was made using 30 pulses (twice the circulation time of the polar emission pattern). We further smooth this pattern over 9 x 9 points in order to reduce the noise, a smaller number of subbearns allowed us more smoothing possible than in B0943+10.

Similar to decameter observations of B0943+10, the intensities of the individual subbeams in the case of B0834+06 fluctuate with time. In fact, they change by almost a factor of 10 between certain short averages. At any given time a few subbeams are seen to dominate the emission. We also observed that the emission from the other parts of the polar cap is greatly reduced during such times. It would appear as if the dominant emission entities inhibit emission from the rest of the polar cap. The emission entities are generally less stable compared to the behavior in the case of B0943+10. The overall average positions of the subbeams remain unchanged, though there is an increased tendency to fluctuate around the mean position in comparison with B0943+10, which may explain the low-Q of the primary fluctuation feature.

Set-2 (5^{th} February 1999)

The polar map for this sequence is shown in figure 5.27. Only a handful of distinct subbeams are seen in the average polar map, whereas short averages corresponding to the frames of the movie show us more distinct subbeams that fluctuate around their mean positions. The subbeam pattern as seen in a movie-frame is distinct, but the brightness of each subbeam seems to fluctuate. Some subbeams seem to attain brightness fluctuations of $\gtrsim 5$ during the movie (a total of ~ 400 pulses) from their maximum to minimum. A pattern of strong, distinct subbeams appears over $\sim 2\hat{P}_3$,

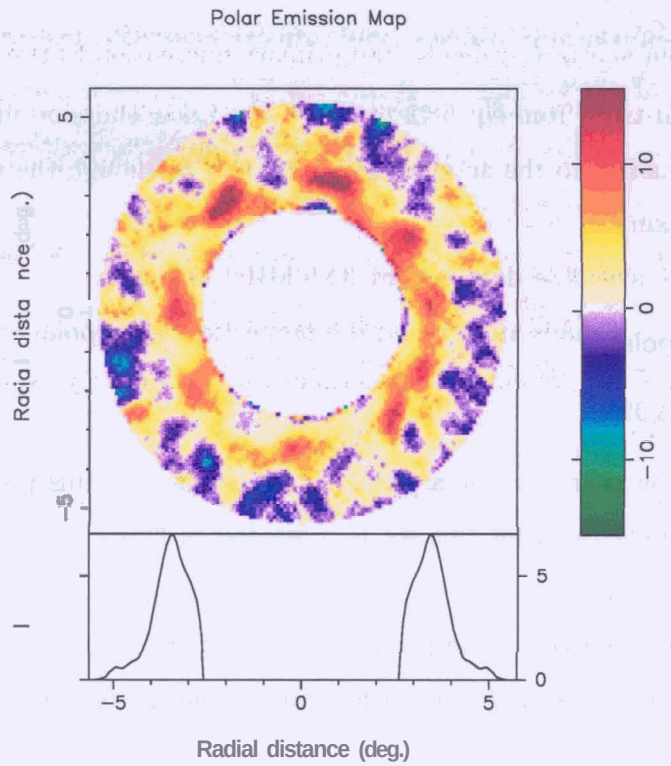

Figure 5.26: Average polar map of emission for B0834+06 set-1 using ~ 350 pulses. The subbeams are less distinct and are not equidistant, which also contributes to the low Q-value of primary fluctuation. Considerable averaging has gone into the making the polar map to improve its signal to noise ratio.

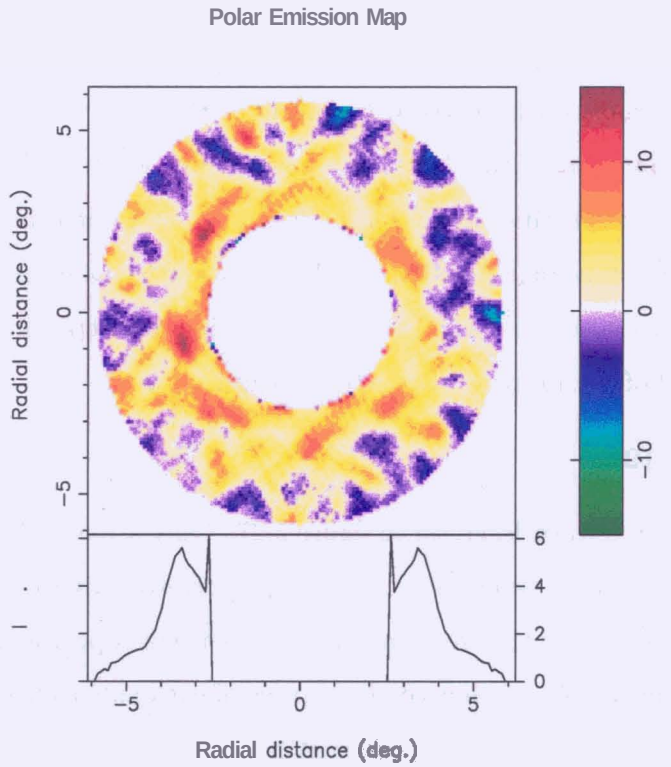

Figure 5.27: Average polar map of emission for B0834+06 set-2 made with 250 pulses.

giving rise to a weak, but sharp (Q-value $\sim$ 100) primary fluctuation feature in the spectra. On the whole a few subbeams dominate polar emission over short durations, similar to the case of set-1. Such 'prominence' last just over one or two circulation times, whence these subbeams weaken and some other subbeams become bright.

The bright subbeams that dominate the emission in a movie frame appear to be broader than the average. Assessing significance of such a result is difficult given the smoothing gone into making movies and the noise present, but sometimes two such nearby bright subbeams appear to nearly merge with each other.

5.5 Discussion and comparison with higher radio-frequency observations

In the preceding sections we presented our analysis of the fluctuation properties apparent in the decametric emission of pulsars B0943+10 and B0834+06, as well as our efforts to understand the underlying emission pattern responsible for them.

Although the signal-to-noige ratio in these observations is insufficient to detect individual pulses, we showed that an estimation of the average fluctuation behavior can still be reliably made, if the magnitude of the fluctuations is high enough to be detected in the data set as a whole. There is an advantage in using a long pulse sequence only if the modulation features are relatively stable over the relevant integration time scales, as in the present case. The primary phase modulation frequency is seen to vary slightly but noticeably, on time scales of many hundreds of the pulse periods.

5.5.1 B0943+10

Pulsar B0943+10 is unusual in that conal narrowing at frequencies above about 400 MHz causes its beam to progressively miss our sightline. For a given β, we expect our sightline to sample the radiation cone at different β/ρ values such that more central traverses occur at lower frequencies. The 'single' profile form of the pulsar at 430 MHz, thus, evolves smoothly into a well defined 'double' form as β/ρ decreases sufficiently at longer wavelengths. The average profile of B0943+10 at 35 MHz exemplifies this situation with an estimated β/ρ of 0.78 (see Table II of Paper-I), corresponding to a nearly complete sampling of the radial 'thickness' (Ap) of the hollow-conical emission pattern. The fractional thickness of this conal beam $\Delta\rho/\rho$ is estimated to be about 15%, consistent with that estimated by Mitra & Deshpande (1999).

The main results of our decametric study of PSR 0943+10's fluctuation properties are as follows:

- We have shown that the fluctuation spectra at decameter wavelengths also display a narrow feature with a high Q close to $0.5\,c/P_1$, which is related to the 'drifting' character of its subpulses.
- We have independently resolved how this feature is aliased and have determined the true frequency of the primary phase modulation.
- The high and low frequency features in the sequence of set-1 were found to be harmonically

related (the former just 20 times the latter). Furthermore, weak sidebands appear to be associated with the primary phase-modulation feature, again suggesting that a slower fluctuation of period $\hat{P}_3 = 20P_3$ is modulating the primary phase fluctuation.

- Since the viewing geometry at 35 MHz is too central ($\beta/\rho = 0.78$) to follow the 'drift' band continuously across the pulse window, we have adopted different means of estimating the value of P_2, which at 11° agrees well with that determined in Paper-I.

- Our observations lead to the conclusion that a system of 20 subbeams, rotating around the magnetic axis of the star with a circulation time $\hat{P}_3$ of about 37 P_1, is responsible for the observed stable subpulse-modulation behavior.

- Compared with the higher frequency maps, the 35-MHz maps sample the subbeams much more completely. However, the 35-MHz subbeams, on the whole, show much less uniformity in their positions and intensities.

- At both 35 MHz and the higher frequencies, the intensities of individual subbeams fluctuate, maintaining a stable brightness only for a few circulation times. The stability time scales of the entire pattern appear roughly comparable between 35 MHz and 430 MHz.

Since the particle plasma responsible for the pulsar emission originates close to 'acceleration' zone (which is considered to be located near the magnetic polar cap), whereas the conversion to radio emission occurs at a height of several hundred kilometers above the stellar surface, we are led to conclude that the polar cap is connected to the region of emission via a set of 'emission columns'. This picture is further supported by the very similar emission patterns observed at 35 MHz and 430 MHz—emitted, presumably, at significantly different altitudes in the star's magnetosphere. If indeed some 'seed' activity results in the common character of the emission patterns at different frequencies, then the parameters describing the fluctuations (*e.g.* P_2, P_3) should be independent of the observing frequency, e.g. as in the model of Ruderman & Sutherland (1975). This expectation is consistent with our observations of B0943+10 (at 35 MHz) and 100 & 430 MHz (Paper-I), as well as with the findings of Nowakowski et *al.* (1982).

The plasma flow in a emission column is guided by the dipolar magnetic field only out a certain distance, but the toroidal field due to the particle currents could become significant away from the star, where low frequency radio waves may be emitted. The lower level of organization, as noted above, in our maps at 35 MHz, as well as "movies", compared to the 430-MHz behavior (Paper-I), may be pointing to this effect.

The average profile at decameter wavelength also shows asymmetry (the peak intensities of the two components around the apparent central longitude differ by a factor of about 2), so also the profile of modulated power (see figure 5.12). Such an asymmetry, though striking, may be traceable to relatively small departures of the polar cap boundary from circularity, if the departures are comparable to the fractional thickness of the emission cone ($\Delta\rho/\rho$). A study, by Arendt & Eilek (2000), of the detailed shape of the polar-cap boundary and its dependence on the inclination angle α, shows that an about 5% departure from circularity is expected for $\alpha = 15°$.

The average profile at decameter wavelength shows asymmetry in the component locations around the chosen magnetic longitude, when fitted with Gaussian profiles. The plot of the amplitude and phase of the primary fluctuation against the pulse longitude shows approximate symmetry around the central longitude. This can now be used to put limits on the possible non-circularity of the subbeam track around the magnetic axis.

Deshpande & Rankin observed a non-fluctuating component in the pulse that was symmetric around the central longitude. We do not detect any non-fluctuating (or randomly fluctuating) 'base' component in our plots of the pulse sequence folded at the primary fluctuation period P_3 (see figure 5.12). We, however, do detect a weak connecting bridge between the two components of the pulse, which is as strong as 20% in one pulse sequence (set-2), and is much weaker in the other (set-1). There is a little or no fluctuation power observed under this component. We would like to argue that it shares a common origin with the non-fluctuating base observed at 430 MHz. Such a component may be a much reduced contribution from a possibly bright central 'core' component and deserves further study.

Among a total of 6 sets at 35 MHz, we find only one sequence exhibiting a 'Q'-mode behavior—that is, with both the average profile and fluctuation spectra displaying clear deviations from 'B'-mode properties. This predominant 'B'-mode character of the decametric emission in our observations, as well as in the earlier observations of Deshpande & Radhakrishnan (1994), appears inconsistent with the trend at higher frequencies where both the 'B' and 'Q' modes may occur with similar frequency of occurrence (Suleymanova et *al.* 1998). It is possible however, that the intervals of disorganized pattern in our observations correspond to some mode-change activity. The weakening of the pulse after the bright phase in the sequence of set-2 may be an indication of a possible B to Q mode change.

5.5.2 B0834+06

We have studied the single-pulse sequences from this pulsar employing much the same techniques that were used in the case of B0943+10.

Apart from B0943+10, B0834+06 is the only other pulsar for which we could estimate the circulation time of the polar emission pattern reliably using the fluctuation properties and its viewing geometry. This estimation is based solely on the decameter observations ! We have made polar emission maps from our data at 34.5 MHz using the estimated $\hat{P}_3$ and drift direction, and those were presented in the earlier section. In carrying out this estimation we followed a general strategy for the estimation of the circulation time of the polar emission pattern. This approach could be adopted in other cases as well. We began with the lrf- and hrf-spectra of this pulsar. We have shown, that

- The primary fluctuation is related to the amplitude modulation of the two components of the average profile.
- The modulation under the pulse displays a time delay between the two components of the profile (see eq. 5.30).
- We would like to argue that the amplitude fluctuations of the two components occur due to the 'passage' of the same emission entity as the entire polar emission pattern revolves steadily around the pulsar's magnetic axis. This, for a component separation of $56°$ in magnetic longitude, suggests the circulation time ($\hat{P}_3$) to be $\sim 14.8\,\mathrm{P}_1$.
- The hrf-spectrum, computed using set-2, displays sidebands around the primary modulation (see figure 5.15). These sidebands imply a slower frequency modulating the primary modulation feature, which has a period of $\sim 14.5 \pm 0.8\mathrm{P}_1$. We notice discernible power in the lrf-spectrum of the same pulse sequence (figure 5.13) at a frequency close to $0.07\,\mathrm{c/P}_1$ (a period of $\sim 14.22 P_1$).
- We believe that these observations conclusively define the circulation time to be $\sim 14.8\,\mathrm{P}_1$.
- The estimates of the viewing geometry in the case of this pulsar are uncertain. We carried out a search to refine the viewing geometry and other parameters of transform using the inverse "Cartographic Transform". This search, for different values of parameters used, constrains the circulation time (now, refined to be $\hat{P}_3 = 14.84\,\mathrm{c/P}_1$) and the drift direction of the pattern relative to the pulsar rotation, so crucial for our mapping technique.

- A system of discrete subbeams in steady rotation along the magnetic axis was responsible for the observed single-pulse fluctuations.

The emission beams in the case of B0834+06 are discrete, but they are not uniformly spaced along the hollow cone of emission and they all differ in their appearance. The subbeams appear broader in radial cross-section, with $\Delta\rho/\rho \gtrsim 25\%$, and seem to fluctuate around their average position and intensity more than those in the case of B0943+10. We had concluded from our analysis of B0943+10 that the regions of radio emission correspond to a well-organized system of plasma columns. In the case of B0834+06, with $a = 30$, we observe a lower order in the polar maps, and higher degree of fluctuations in the subbeam locations and their brightness. The increased jitters in the subbeam position could result in the low Q-value of the observer fluctuation features. It was not possible to account for the null pulses, which could further reduce the modulation Q.

We also made maps from successive subsections of the pulse sequence and viewed them in a 'movie'-like fashion. The subbeams in the case of B0834+06 display a higher degree of fluctuation in their brightness and position on the polar cap as compared to B0943+10. In fact, usually a couple of bright subbeams dominate the polar cap emission. One may think of two plausible explanations in this regard: a] The subbeams of emission compete with each other in such a way, that inhibition of emission (or the underlying sparks) would occur over the rest of the polar cap when some subbeams are active (a theoretical conjecture by R&S for discrete subbeams, and a more explicit suggestion by Vivekanand & Joshi (1999) in their study of B0031-07). b] Formation of a steady, bright subbeam pattern on the polar region may require certain physical conditions which may be satisfied in a small region of pulsar-parameter space (consisting of viewing geometry and rotational parameters of the neutron star). It may seem that such conditions indeed conspire to generate stable pattern of 20 subbeams observed in the case of meter-wave emission from B0943+10. The above two possibilities are certainly due to some underlying physical cause.

This analysis has been done using the data obtained at 34.5 MHz alone and we do not have any polar emission maps made using single-pulse sequences at meter-wavelengths for a comparison. We believe that such a structure of discrete subbeams is valid even at higher frequencies, where strong, alternate pulse modulation of moderate Q-value has been observed. A more direct comparison between emission at decameter and meter wavelengths is possible in this case, and would prove fruitful.

The importance of our analysis also lies in the fact, that pulsar B0834+06 is *different* from B0943+10 in its physical parameters, the viewing geometry, as well as the nature of the

apparent modulation due to drift. The single-pulse fluctuations in this case are general modulation of component amplitudes, unlike a stable drift pattern observed in the case of B0943+10. Even for such a case of general modulation we could relate it to a well-defined rotating pattern in the polar emission region. This further supports our belief that a set of discrete subbeams of emission, as envisioned in R&S, result in single-pulse fluctuations in pulsars, and their apparent nature is a combination of the pulsar parameters and the observer's viewing geometry.

5.5.3 Comparison with theory : number of sparks *vs.* α, β, and other parameters

Overall, our observations of B0943+10 and B0834+06 agree remarkably with the picture of a steady system of discrete emission subbeams in an apparent circulation around the magnetic axis. This cartoon has a remarkable overlap with the R&S model articulated at the beginning of this chapter.

R&S provided a comprehensive picture of discrete sparks on the polar cap of a pulsar, which undergo an E x B drift around the magnetic axis, giving rise to the observed subpulse drift pattern. The size of the polar cap is given by eq. 5.4 to be ~ 100 m. The circulation time of the spark, situated at a radial distance r_s from the center of the polar cap, with the drift velocity of E x $\mathbf{B}/B^2$ can be written as, $\hat{P}_3 = 2\pi r_p (B/ < \mathrm{E} >) P_1$, where B and $< \mathrm{E} >$ are the magnetic field and average radial electric field in the gap. $< \mathrm{E} >$, in turn can depends upon the potential drop in the gap AV and the spark distance from the edge of the polar cap $(r_p - r_s)$. From R&S, eq.[30], $< \mathrm{E} >= \Delta V/2(r_p - r_s)$ (see DRa). The circulation time then becomes,

$$\hat{P}_3 = 4\pi r_s (r_p - r_s) B / \Delta V P_1. \qquad (5.43)$$

R&S assume $r_s = r_p/2$, and derive their relation for the circulation time (eq. 5.22). Deshpande & Rankin argue for $r_s \sim r_p$, and AV considerably smaller than 10^{12} to explain the long circulation time in the case of B0943+10 (DRa).

We tabulate all the relevant parameters of these two pulsars in table 5.3, where the magnetic field estimates are derived from their timing behavior. How do the observed numerical values compare with the theoretical estimates?

The estimated circulation time, number of subbeams, and their temporal behavior differ for the two pulsars. The exact theoretical estimation of $\hat{P}_3$ using eq. 5.21 is obscure due to uncertainties in surface parameters such as the radius of curvature of the field lines in the emission region and the voltage drop across the gap.

Instead of the actual values of $\hat{P}_3$, we compare the estimates of $\hat{P}_3$ as given by eq. 5.22 for

Pulsar	α	β	B_{12}	P_1 s	number of subbeams	P_3 (in P_1)	$\hat{P}_3$ (R&S) (in P_1)	$\hat{P}_3$ (obs) (in P_1)	$\hat{P}_3$ s
B0943+10	11°.64	−4°.31	2.0	1.0977	20	1.848	9.3	36.95	40.57
B0834+06	30°.00	−3°.00	3	1.2738	8	1.855	13.1	14.84	18.9

Table 5.3: Comparison between the observed circulation time and theoretical estimates of R&S model. The various pulsar parameters for B0943+10 and B0834+06 are listed.

the two pulsars, and write

$$\left(\frac{(\hat{P}_3)_{0943+10}}{(\hat{P}_3)_{0834+06}}\right)_{estimated} = K\left(\frac{(\hat{P}_3)_{0943+10}}{(\hat{P}_3)_{0834+06}}\right)_{observed} \tag{5.44}$$

with K=1, if the constant multiplier (of value 5.6) in the eq. 5.22 remains unchanged from one pulsar to another. We, however, find the value of K to be 0.29, which suggests that this multiplier value is dependent on pulsar parameters.

5.6 Summary

In this chapter, we presented our analysis of the single-pulse fluctuations observed in the decametric emission of pulsars B0943+10 and B0834+06 in detail and tried to understand the observed diverse single-pulse fluctuation properties in terms of polar emission patterns and their temporal behavior. We compared our observations with the general picture of radio emission patterns and subpulse modulation elaborated theoretically by Ruderman & Sutherland (1975) and to the higher frequency observational results of Deshpande & Rankin (DRa and paper-I).

We described the theoretical picture suggested by Ruderman & Sutherland in the beginning. We studied the fluctuation features of the two pulsars in detail. The technique of 'Cartographic Transform', where every sample from each single pulse is uniquely mapped onto the polar region of the pulsar, provides new means of studying underlying emission patterns using single-pulse phenomena. We discussed the various issues related to this technique and used it to obtain polar emission maps for these two pulsars.

Although the signal-to-noise ratio in these observations was insufficient to detect individual pulses, we showed that an estimation of the average fluctuation behavior can still be made reliably, if the magnitude of fluctuations is high enough to be detected in the data set as a whole. There is an advantage in using a long pulse sequence only if the modulation features are relatively stable over the relevant integration time scales, as in the present case.

In the case of **B0943+10**, our observations lead to the conclusion that a system of 20 subbeams, rotating around the magnetic axis of the star with a circulation time $\hat{P}_3$ of about 37 P_1 is responsible for the observed stable subpulse-modulation behavior. Compared with the higher frequency maps, the 35-MHz maps sample the subbeams much more completely in their radial extent However, the 35-MHz subbeams, on the whole, show much less uniformity in their positions and intensities. At both, 35 MHz and the higher frequencies, the intensities of individual subbeams fluctuate, maintaining a stable brightness only for a few circulation times. The stability time scales of the entire pattern appear roughly comparable between 35 MHz and 430 MHz.

Since the particle plasma responsible for the pulsar emission originates close to 'acceleration' zone (which is considered to be located near the magnetic polar cap), whereas the conversion to radio emission occurs at a height of several hundred kilometers above the stellar surface, we are led to conclude that the polar cap is connected to the region of emission via a set of 'emission columns'. This picture is further supported by the very similar emission patterns observed at 35 MHz and 430 MHz—emitted, presumably, at significantly different altitudes in the star's magnetosphere.

We, detect a weak connecting bridge between the two components of the pulse, which is as strong as 20% in one pulse sequence (set-2), and is much weaker in the other (set-1). There is a little or no fluctuation power observed under this component. We would like to argue that it shares a common origin with the non-fluctuating 'base' component observed at 430 MHz. Such a component may be associated with a much reduced contribution from a possibly bright central 'core' component and deserves further study. Among a total of 6 sets at 35 MHz, we find only one sequence exhibiting a 'Q'-mode behavior—that is, with both the average profile and fluctuation spectra displaying clear deviations from 'B'-mode properties. This predominant 'B'-mode character of the decametric emission in our observations as well as in the earlier observations of Deshpande & Radhakrishnan (1994) is in significant contrast with the trend at higher frequencies where both the 'B' and 'Q' modes may occur with similar frequency of occurrence (Suleymanova et *al.*1998).

B0834+06 is the only other pulsar, apart from B0943+10, for which we could estimate the circulation time of the polar emission pattern reliably using the fluctuation properties and its viewing geometry. This estimation is based solely on the decameter observations ! We have made polar emission maps from our data at 34.5 MHz using the estimated $\hat{P}_3$ and drift direction and those were presented in the earlier section. In carrying out this estimation we followed a somewhat general strategy for the estimation of the circulation time of the polar emission pattern. This approach, mentioned below, could be adopted in other cases as well.

We studied the fluctuation modulations of this pulsar. The modulation under the pulse displays a time delay between the two components of the profile. We argued that the amplitude fluctuations associated with each of the two components occur due to the 'passage' of the same emission entity as the entire polar emission pattern revolves steadily around pulsar's magnetic axis. This understanding then allows us to scale the time delay associated with a component separation of some $\delta\zeta$ in magnetic longitude (corresponding to the profile component separation of $\delta\varphi$), thus providing the initial guess for the circulation time. We searched our fluctuation spectra for slow modulation features with frequencies close to this 'guess' of circulation time. We further carried out a search to refine the viewing geometry and other parameters of transform using the inverse of "Cartographic Transform". This method yielded a refined determination of the circulation time and drift direction of the pattern relative to the pulsar rotation, both so crucial for our mapping technique.

Here too, a system of discrete subbeams in steady rotation along the magnetic axis was found responsible for the observed single-pulse fluctuations. The emission beams in the case of B0834+06 are discrete, but they are **not** uniformly spaced along the hollow cone of emission and

they all differ from each other in their appearance. The subbeams appear broader in radial cross-section, with $\Delta\rho/\rho \gtrsim 25\%$, and seem to fluctuate around their average position and intensity more than what was observed in the case of B0943+10.

The increased jitters in the subbeam position could result in the low Q-value of the observed fluctuation features. Also, it was not possible to account for the null pulses, which could further reduce the modulation feature's Q.

We also made maps from successive subsections of the pulse sequence and viewed them in a 'movie'-like fashion. For all the data sets of B0943+10 and B0834+06 discussed, it was noticed that only a few subbeams (different ones at different times) usually dominated in intensity over a few circulation times. Overall, the brightness of a given subbeam was observed to fluctuate by up to about a factor of **4** over the length of the sequence. Given the above, it is tempting to suggest that (a) an inhibition of emission (or the underlying sparks) occurs over the rest of the polar cap due to the active subbeams, or (b) **A** critical combination of parameters required for stable, uniform subbeams.

It is important to note, that that pulsar B0834+06 is ***different*** from B0943+10 in its physical parameters, the viewing geometry, as well as the nature of the apparent modulation due to drift. The single-pulse fluctuations in this case are general modulation of component amplitudes, unlike the stable 'drift' patterns observed in the case of B0943+10. Even such a general amplitude modulation appears to be related to a well-defined rotating pattern in the polar emission region. This further supports our view that a set of discrete subbeams of emission and their apparent circulation, as envisioned in R&S, results in the single-pulse fluctuations observed. The apparent nature of the modulation is a combination of the pulsar parameters and the observer's viewing geometry.

Overall, our observations of B0943+10 and B0834+06 agrees remarkably with the picture of a steady system of discrete emission subbeams in an apparent circulation around the magnetic axis. This cartoon has a remarkable overlap with the R&S model. When we compare the results for the two pulsars, the observed value of the circulation time of B0834+06 is considerably shorter than that expected from the model.